bioRxiv preprint doi: https://doi.org/10.64898/2026.01.20.700679; this version posted January 20, 2026. The copyright holder for this preprint (which was not certified by peer review) is the author/funder, who has granted bioRxiv a license to display the preprint in perpetuity. It is made available under a CC-BY 4.0 International license.

Decoding the cell intrinsic and extrinsic roles of PRC2 in early embryogenesis

Chengjie Zhou[1,2,†], Meng Wang[1,2,†], Zhiyuan Chen[1,2,3,4], Yi Zhang[1,2,5,6,7,*]

Affiliations:

[1]Howard Hughes Medical Institute, Boston Children's Hospital, Boston, MA 02115, USA.

[2]Program in Cellular and Molecular Medicine, Boston Children's Hospital, Boston, MA 02115, USA.

[3]Reproductive Sciences Center, Division of Developmental Biology, Cincinnati Children's Hospital Medical Center, Cincinnati, OH 45229, USA.

[4]Department of Pediatrics, University of Cincinnati College of Medicine, Cincinnati, OH 45267, USA.

[5]Division of Hematology/Oncology, Department of Pediatrics, Boston Children's Hospital, Boston, MA 02115, USA

[6]Department of Genetics, Harvard Medical School, Boston, MA 02115, USA.

[7]Harvard Stem Cell Institute, Boston, MA 02115, USA.

* Corresponding author. Email: yzhang@genetics.med.harvard.edu

† These authors contributed equally to this work.

Key words: Polycomb, H3K27me3, maternal-to-zygotic transition, epiblast specification, primordial germ cells

Manuscript information: 54 pages, 7 Figures, 7 Extended Data Figures, 7 Supplemental Tables

bioRxiv preprint doi: https://doi.org/10.64898/2026.01.20.700679; this version posted January 20, 2026. The copyright holder for this preprint (which was not certified by peer review) is the author/funder, who has granted bioRxiv a license to display the preprint in perpetuity. It is made available under a CC-BY 4.0 International license.

Abstract

Early embryogenesis is accompanied by dynamic epigenetic modifications. While such dynamics are important in cell intrinsic regulation of gene expression, their extrinsic roles in mediating intercellular communication during early embryogenesis is less understood. Using the protein degradation tag (dTAG) system, here we decode stage- and lineage-specific functions of *Eed*, a core component of Polycomb Repressive Complex 2 (PRC2) in mouse early embryogenesis. Our results reveal previously underappreciated cell intrinsic and extrinsic functions of PRC2 in regulating pre-implantation and primordial germ cell (PGC) development, respectively. We demonstrate that PRC2 is required for normal maternal to zygotic transition (MZT), and epiblast (EPI) specification. Moreover, PRC2 controls proper PGC numbers in EPI through a PRC2-ESRRB-BMP4 regulatory axis in extraembryonic ectoderm (ExE). Thus, our study uncovers a previously unknown cell-autonomous function of PRC2 in preimplantation development and its non-cell-autonomous function in PGC number regulation, both through interplays between epigenetic-epigenetic and epigenetic-TFs networks.

bioRxiv preprint doi: https://doi.org/10.64898/2026.01.20.700679; this version posted January 20, 2026. The copyright holder for this preprint (which was not certified by peer review) is the author/funder, who has granted bioRxiv a license to display the preprint in perpetuity. It is made available under a CC-BY 4.0 International license.

Introduction

Following fertilization, embryonic development initially relies on the maternal products inherited from eggs and gradually becomes dependent on the newly synthesized zygotic products [1]. In the mouse, awakening of the zygotic genome takes places in two waves. The minor wave starts at late 1-cell stage with hundreds of genes transcribed, whereas the major wave starts at late 2-cell stage with thousands of genes activated [2-4]. The maternal RNA decay and zygotic genome activation (ZGA) together are known as maternal-to-zygotic transition (MZT) [1,5]. During MZT, the embryonic genome is also subject to extensive epigenetic reprogramming to erase germ cell signatures and to acquire totipotency. After a few rounds of cell cleavages, embryonic cells gradually lose totipotency and undergo the first cell fate specification at embryonic day (E) 3.5 to form inner cell mass (ICM) and trophectoderm (TE) lineages [6-9]. During the second lineage specification at E4.5, the ICM cells become epiblast (EPI), which marks the establishment of naïve pluripotency [10], and primitive endoderm (PrE). Following implantation, the EPI exits from naïve pluripotency and acquires the formative pluripotency at E5.5 and transforms to the primed pluripotency at E6.5 [11]. Meanwhile, the specification of primordial germ cells (PGCs) from EPI occurs as early as E6.25 [12].

Polycomb group (PcG) proteins play a fundamental role in mediating epigenetic silencing in multiple biological processes including embryonic development, genomic imprinting, X-chromosome inactivation (XCI), and cancer progression [13-16]. PcG proteins form two major complexes that differentially contribute to Polycomb-mediated gene silencing. The Polycomb Repressive Complex 1 (PRC1) contains the E3 ubiquitin ligases RING1A/RING1B to deposit mono-ubiquitin to lysine 119 of histone H2A in mammals (H2Aub)[17,18], whereas the PRC2 methyltransferases EZH1/2 catalyze mono-, di-, and tri-methylation at lysine 27 of histone 3 (H3K27me1/2/3)[19-22]. Essential roles of PRC2 in embryonic development have been previously established by functional studies. Zygotic knockout (KO) of the core subunits of PRC2 (*e.g., Eed, Ezh2,* and *Suz12*) indicate that PRC2 are essential for proper gastrulation but largely dispensable for preimplantation development [23-25]. Depletion of maternally inherited PcG proteins requires conditional KO that starts at early stage of oogenesis (*i.e.,* postnatal day 3-5). Loss of maternal PRC2 has a milder effect on postnatal oogenesis despite having some effects on oocyte transcriptome [26], but mainly affects non-canonical imprinting, imprinted XCI, and post-implantation development [27-33]. While the maternal and zygotic KOs of PRC2 have provided important insights into PRC2's functions in germline and early post-implantation development, neither approach can capture the initial and direct effect caused by PRC2 loss in pre- and post-implantation embryos. On one hand, the zygotic KO may underestimate Polycomb function before embryo implantation due to maternal compensations. On the other hand, for the conditional KOs

bioRxiv preprint doi: https://doi.org/10.64898/2026.01.20.700679; this version posted January 20, 2026. The copyright holder for this preprint (which was not certified by peer review) is the author/funder, who has granted bioRxiv a license to display the preprint in perpetuity. It is made available under a CC-BY 4.0 International license.

starting at early stage of oogenesis, potential zygotic compensatory and/or secondary effects may accumulate overtime and complicate interpretations of phenotypes detected in preimplantation embryos.

To address these technical limitations, here we applied the protein degradation tag (dTAG) system [34,35] to systematically evaluate the PRC2 function throughout mouse pre- and early post-implantation development. In this approach, the endogenous EED, a PRC2 core subunit, is fused to the degradation tag so that it can undergo inducible and rapid degradation. We showed that the dTAG system enables rapid and efficient depletion of both EED and H3K27me3 in both pre- and early post-implantation embryos. Through stage-specific PRC2-depletion studies, we reveal previously underappreciated functions of PRC2 in regulating key events in early embryonic development including maternal-to-zygotic transition (MZT), the first and second cell lineage specifications, as well as PGC development. Our results indicate that PRC2 is required for normal MZT and is essential for ensuring proper EPI formation by preventing premature activation of later-stage developmental genes at E4.5 ICM. In addition, we show that the H3K27me3 and H3K4me3 bivalency established at E4.5 ICM *in vivo*, which is earlier than previously thought of its establishment after implantation [36]. Importantly, we demonstrate that PRC2 regulates *Bmp4* expression through a PRC2-ESRRB-BMP4 regulatory axis in extraembryonic ectoderm (ExE), which controls proper PGC numbers through a crosstalk with EPI cells. These results demonstrate that PRC2 exhibits multi-faced stage-specific functions through dual interplay with epigenetic and transcription factors during early embryonic development.

bioRxiv preprint doi: https://doi.org/10.64898/2026.01.20.700679; this version posted January 20, 2026. The copyright holder for this preprint (which was not certified by peer review) is the author/funder, who has granted bioRxiv a license to display the preprint in perpetuity. It is made available under a CC-BY 4.0 International license.

Results

Targeted protein degradation reveals that PRC2 regulates preimplantation development

A comprehensive analysis of the expression patterns of PRC2 components revealed that most of them are expressed throughout pre- and peri-implantation development (**Fig. 1a**). Similarly, an analysis of our previous low-input ribosome profiling dataset also indicated that these mRNAs are translated in preimplantation embryos **(Extended Data Fig. 1a**) [37]. Consistently, immunostaining analyses detected H3K27me3 and the core subunit EED from early 1-cell (before ZGA) to blastocyst stage (**Fig. 1b**). The EED and H3K27me3 signals increase at 2-cell stage (when ZGA occurs) and exhibit higher intensity in the ICM than the TE at blastocyst stage (**Fig. 1b and Extended Data Fig. 1b, c**). This 2-cell increase and ICM-biased enrichment of EED and H3K27me3 are consistent with a prior report [38], and suggest a potential role of PRC2 in ZGA and lineage specification during mouse preimplantation development.

To systematically address the function of PRC2 at different stages of early embryogenesis, we established an *Eed* dTAG model with a *Fkbp12*^{F36V}*-V5* degron inserted before the stop codon of the endogenous *Eed* locus (**Extended Data Fig. 1d**). In the presence of the small molecule dTAG13, EED-FKBP12^{F36V}-V5 fusion protein, referred to as EED-dTAG, is expected to be poly-ubiquitinated and rapidly degraded by proteosomes. We first confirmed in mouse embryonic stem cells (mESCs) that the EED-dTAG is stable without dTAG13 but undergoes rapid degradation in 30 mins upon dTAG13 treatment (**Fig. 1c and Extended Data Fig. 1e**). We further established a mouse knock-in founder line by co-injecting Cas9 mRNA, the sgRNA, and the donor DNA into the cytoplasm of 2-cell embryos (**Fig. 1d**) as microinjection at 2-cell stage enhances knock-in efficiency [39]. Indeed, a high percentage of injected blastocysts (56.5%, 13 out of 23) showed mosaic V5 tag signals (**Fig. 1d**), suggesting successful knock-in. Importantly, the *Eed* dTAG homozygous knock-in mice, referred to as *Eed*$^{dTAG/dTAG}$, are viable and fertile (**Extended Data Fig. 1f**), suggesting that the EED-dTAG fusion protein function equivalently as the wild type EED.

To evaluate the depletion efficiency in embryos, *Eed*$^{dTAG/dTAG}$ embryos were cultured *ex vivo* with or without the presence of dTAG13 from early 1-cell (6 hpf, 6 hr post fertilization) to early (20 hpf, corresponding to minor ZGA) or late 2-cell (30 hpf, corresponding to major ZGA) stages. Immunostaining analyses showed that EED were near completely depleted by early and late 2-cell stages (**Fig. 1e and Extended Data Fig. 1g-i**), indicating a rapid and efficient degradation. Notably, H3K27me3 was also nearly undetectable upon dTAG13 treatment (**Fig. 1e and Extended Data Fig. 1g-i**), suggesting active demethylation taking place in the absence of PRC2 at these stages. These data indicate that we have successfully established a dTAG mouse model that enables rapid and efficient depletion of EED and H3K27me3 in preimplantation embryos.

bioRxiv preprint doi: https://doi.org/10.64898/2026.01.20.700679; this version posted January 20, 2026. The copyright holder for this preprint (which was not certified by peer review) is the author/funder, who has granted bioRxiv a license to display the preprint in perpetuity. It is made available under a CC-BY 4.0 International license.

We next sought to determine whether rapid depletion of EED at different stages impact preimplantation development. Specifically, *Eed*$^{dTAG/dTAG}$ embryos were cultured with dTAG13 from zygotes to blastocyst stage, from zygotes to 4-cell stage, or from 4-cell to blastocyst stage (**Fig. 1f**). Remarkably, all treatment groups impaired blastocyst formation with the first group showing the strongest effect (~33% blastocyst rate decrease) (**Fig. 1g, h**). This defect is more severe than the previously reported *Eed* maternal KO that caused post-implantation defects [29,31], which could be due to the effective depletion of both maternal and zygotic EED in the current study. Furthermore, *Eed*$^{dTAG/dTAG}$ embryos cultured with dTAG13, irrespective of different treatment windows, showed reduced ICM (OCT4^{+}/CDX2^{-}) and TE (CDX2^{+}) cells (**Fig. 1i-k**). Collectively, these data suggest a previously unappreciated role of PRC2 in preimplantation development.

PRC2 regulates MZT and represses a few developmental genes during ZGA

To gain mechanistic understanding of how PRC2 regulates preimplantation development, we attempted to reveal transcriptome changes caused by EED depletion at different developmental stages. At late 2-cell stage, ZGA and maternal RNA decay are largely completed. These two events together are known as maternal-to-zygotic transition (MZT) and are essential for embryonic development [1] . Given that EED loss from zygote to 4-cell stage impaired blastocyst formation (**Fig. 1g-k**), PRC2 might function during MZT. To determine how EED loss might affect MZT, RNA-seq was performed for the *Eed*$^{dTAG/dTAG}$ early and late 2-cell embryos cultured in the presence or absence of dTAG13 (**Fig. 2a, b and Extended Data Fig. 2a, b**). RNA-seq indicated that acute depletion of EED had minimal impact on transcriptome at the early 2-cell stage (**Fig. 2a**), but it caused 350 and 244 genes up- and down-regulated, respectively, at the late 2-cell stage (**Fig. 2b and Supplementary Table 1, 2**). The up- and down-regulated genes are enriched for maternal genes and ZGA genes, respectively (**Fig. 2c-e and Supplementary Table 1, 2**), suggesting a MZT defect. However, acute loss of EED had little effect on the expression of transposable elements (**Extended Data Fig. 2c**). Collectively, these data suggest that EED acute depletion does not affect minor ZGA but causes defects in major ZGA and maternal decay at the late 2-cell stage.

To identify potential direct targets of EED, the differentially expressed genes were compared to the late 2-cell H3K27me3 profiling data [40], with Hox genes and housekeeping genes serving as H3K27me3-positive and -negative control loci, respectively (**Extended Data Fig. 2d**). We identified a few developmental genes (*e.g., Homer2* and *Tex101*), metabolic genes (*e.g., Clu* and *Eno1b*), and immune genes (*e.g., Ifitm1* and *Cd40*) that are enriched for H3K27me3 and ectopically de-repressed upon acute EED depletion (**Fig. 2f**). These data support that H3K27me3 is retained at some developmental genes and is essential for keep them repressed during ZGA.

bioRxiv preprint doi: https://doi.org/10.64898/2026.01.20.700679; this version posted January 20, 2026. The copyright holder for this preprint (which was not certified by peer review) is the author/funder, who has granted bioRxiv a license to display the preprint in perpetuity. It is made available under a CC-BY 4.0 International license.

PRC2 regulates lineage-specific genes during mid-preimplantation development

After ZGA, embryos exit totipotency by downregulating the 2-cell specific totipotent genes and then initiates the first lineage specification during embryo compaction at the 8-cell stage [6,8]. Since acute depletion of EED affected both ICM and TE cell numbers in blastocysts (**Fig. 1i-k**), we next sought to understand how EED/PRC2 may regulate the first lineage specification. To avoid the potential secondary effects caused by EED loss during ZGA at the 2-cell stage (**Fig. 2a**), *Eed*$^{dTAG/dTAG}$ embryos were cultured with dTAG13 from 4-cell (45 hpf) to morula stage (72hpf), when cells have undergone compaction (**Fig. 2g**). Immunostaining analyses revealed that both EED and H3K27me3 were completely depleted at morula stage (**Fig. 2g**). Comparative transcriptome analyses identified 156 and 107 genes were up- and down-regulated, respectively, in response to dTAG13 treatment (**Fig. 2h, Extended Data Fig. 2e and Supplementary Table 2**). Interestingly, the well-known pluripotency genes (*i.e., Sox2* and *Nanog*) and trophoblast genes (*i.e., Cdx2* and *Gata3*) were downregulated in the dTAG group (**Fig. 2i**). Indeed, the down-regulated genes were enriched for gene ontology (GO) term "stem cell differentiation" (**Fig. 2j**). The up-regulated genes were enriched for "allantoin metabolic process" and "synaptonemal complex assembly", which are developmental processes that should normally occur in later development (**Fig. 2j, k**). In addition, a subset of totipotent genes became reactivated at the morula stage upon EED loss (**Extended Data Fig. 2f**), suggesting a potential defect in totipotency exit. Taken together, these data support that PRC2-mediated transcriptional silencing during mid-preimplantation development plays an important role in ensuring proper lineage-specific gene expression in compacted morula embryos.

PRC2 regulates EPI formation by preventing premature activation of developmental genes

Given that EED depletion impairs blastocyst formation (**Fig. 1g-h**) and regulates lineage-specific genes during compaction (**Fig. 2i**), we asked whether PRC2 could also regulate the second lineage specification. To avoid indirect effects caused by EED loss in early- and mid- preimplantation development, *Eed*$^{dTAG/dTAG}$ embryos were cultured with dTAG13 starting from morula (72 hpf) or mid-blastocyst (96 hpf) to late-blastocyst stage (112 hpf) (**Fig. 3a**). Both treatment windows nearly completely depleted both EED and H3K27me3 (**Fig. 3b**). Remarkably, acute loss of EED causes reduced percentage of EPI (NANOG^{+}/GATA4^{-}), but not PrE cells (GATA4^{+}/NANOG^{-}) (**Fig. 3c, d**), indicating that EED is essential for EPI specification.

To understand the underlying mechanisms, E4.5 ICM cells were isolated by immuno-surgery [41] and subjected to RNA-seq analyses. Comparative analyses revealed more profound transcriptome changes caused by EED loss at this stage than at the 2-cell and morula stages: with 850 and 668 genes being up-

bioRxiv preprint doi: https://doi.org/10.64898/2026.01.20.700679; this version posted January 20, 2026. The copyright holder for this preprint (which was not certified by peer review) is the author/funder, who has granted bioRxiv a license to display the preprint in perpetuity. It is made available under a CC-BY 4.0 International license.

and down-regulated, respectively (**Fig. 3e, Extended Data Fig. 3a and Supplementary Table 3**). GO term analyses revealed that the up-regulated genes are enriched for developmental processes such as "embryonic organ morphogenesis" and "ossification" (**Fig. 3f**). These GO terms are different from those enriched for the de-repressed genes at morula stage upon acute EED loss (**Fig. 2j**), suggesting that PRC2 represses distinct gene sets at different developmental stages. While EED depletion at this stage does not affect pluripotency gene markers such as *Nanog* and *Sox2* (**Extended Data Fig. 3b**), the formative pluripotency (a transition between naïve and primed pluripotency) marker genes, such as *Otx2* and *Tcf15* are up-regulated by EED depletion (**Fig. 3g**). This data suggests that PRC2 prevent premature activation of genes responsible for naïve- to-formative pluripotency transition. In addition, differentiation markers (*i.e., Meg3* and *Sox11*) and Hox genes, which supposed to be expressed at primed EPI or gastrulation stages were up-regulated when EED was depleted (**Fig. 3g**). Importantly, all these genes are directly repressed by H3K27me3 (**Fig. 3h and Extended Data Fig. 3c, d**). Collectively, these data indicate that PRC2 is essential for EPI formation by preventing premature activation of developmental genes.

PRC2 constrains H3K4me3 levels in E4.5 ICM

We next attempted to connect chromatin changes and the transcriptome dysregulations caused by EED depletion in E4.5 ICM. Analyses of the H2Aub and H3K4me3 changes indicated that EED depletion did not affect global H2Aub profile deposited by PRC1 (**Fig. 3i, j and Extended Data Fig. 3e, f**). This observation is consistent with our previous observation that non-canonical PRC1 deposits the majority of H2Aub independent of PRC2 from oocytes to 4-cell embryos [42]. Notably, EED depletion caused an increase in H3K4me3 at PRC2 targeted genes, where H3K27me3 was highly enriched ("Up1" group in Fig. 3i), but to a much less extent for the H3K27me3 lowly enriched genes ("Up2" group in Fig. 3i) (**Fig. 3i, j and Extended Data Fig. 3f**), suggesting a direct effect on H3K4me3. However, loss of EED did not affect chromatin accessibility as revealed by ATAC-seq (**Fig. 3i and Extended Data Fig. 3f**), suggesting that the increase in H3K4me3 was independent of chromatin accessibility. In addition, *Hox* genes also showed an increase in H3K4me3 and RNA levels in the dTAG group (**Fig. 3k, l and Extended Data Fig. 3f**). These data suggest that PRC2 constrains H3K4me3 and prevents activation of PRC2 targets in E4.5 ICM.

PRC2 plays critical role for bivalency establishment in E4.5 ICM

The fact that both H3K27me3 and H3K4me3 are enriched in developmental genes like *Otx2* and *Bmp2k* at E4.5 ICM (**Fig. 3i, j**) suggests a bivalency state [43]. Previous studies suggest that bivalency is largely absent or infrequent from developmental genes in preimplantation embryos (up to E3.5 ICM) but appears after implantation (E5.5-E6.5 EPI) [36,40]. This inconsistency prompted us to further analyze H3K27me3 and H3K4me3 datasets throughout pre- and post-implantation development to identify bivalent genes

bioRxiv preprint doi: https://doi.org/10.64898/2026.01.20.700679; this version posted January 20, 2026. The copyright holder for this preprint (which was not certified by peer review) is the author/funder, who has granted bioRxiv a license to display the preprint in perpetuity. It is made available under a CC-BY 4.0 International license.

(Methods). This analysis confirmed the largely absence of bivalency before E4.5 ICM, with only 272 and 364 bivalent promoters in 8-cell and E3.5 ICM, respectively (**Fig. 4a-c**). However, a major transition occurs between E3.5 to E4.5 with a ~4-fold increase (1,457 vs. 364) of bivalent genes by E4.5 ICM (**Fig. 4c and Supplementary Table 4**). The number of bivalent genes further increased to 4,382 by E6.5 EPI. Consistent with the notion that bivalency is to poise for activation, the bivalent genes identified are mostly not expressed or lowly expressed in E4.5 ICM and E6.5 EPI (**Extended Data Fig. 4a, b and Supplementary Table 4**).

We next sought to understand how these major transitions of bivalency took place in E4.5 ICM and E6.5 EPI. Clustering analyses revealed that gain of bivalency in E4.5 ICM is mainly due to the further increase in both H3K27me3 and H3K4me3 (**Fig. 4d,** "E4.5 ICM specific"). Note that this group of genes already showed moderate and/or weak enrichment of both modifications in E3.5 ICM. In contrast, only a small percentage (194 out of 1457, 13.3%) of bivalent genes are inherited or maintained from E3.5 to E4.5 ICM (**Fig. 4d,** "Shared"). Unlike the E3.5 to E4.5 ICM transition, the gain of bivalency from E4.5 ICM to E6.5 EPI was mainly due to the increase of H3K4me3 and the inheritance of H3K27me3 at the transcription start sites (**Fig. 4e**). The bivalent genes of all the groups are enriched for similar GO terms such as cell fate commitment and embryonic organ morphogenesis (**Extended Data Fig. 4c, d**). Consistent with earlier analyses (**Fig. 3i**), EED depletion caused increased H3K4me3 at bivalent genes in E4.5 ICM, even including those that normally gain H3K4me3 in E6.5 EPI (**Fig. 4f,** "E6.5 EPI specific"). Furthermore, the increase of H3K4me3 at bivalent genes correlated with their increased expression (**Fig. 4g**), with a stronger effect for genes already show high levels of H3K4me3 in E4.5 ICM ("E4.5-specific" and "Shared") (**Fig. 4h**).

Collectively, these analyses reveal a more complete picture of how bivalency is established in pre- and early post-implantation embryos. In preimplantation embryos, H3K4me3 is weakly present at promoters as early as 4-cell to 8-cell stage, and H3K27me3 is initially deposited in the E3.5 ICM. Both markers are subsequently further increased in the E4.5 ICM to establish bivalency. In contrast, in early post-implantation embryos, H3K27me3 is first primed in the E4.5 ICM, while H3K4me3 is deposited later in the E6.5 EPI to finally establish bivalency (**Fig. 4i**). These data also demonstrate that PRC2 constrains H3K4me3 and transcription levels at bivalent genes in E4.5 ICM (**Fig. 4j**).

PRC2 restricts PGC numbers by repressing BMP4 signaling through a lineage crosstalk

We further explored the role of PRC2 in regulating bivalency genes in post-implantation embryos. To this end, we first confirmed that the dTAG system can rapidly and efficiently degrade EED (~4 hr) in *ex vivo*

bioRxiv preprint doi: https://doi.org/10.64898/2026.01.20.700679; this version posted January 20, 2026. The copyright holder for this preprint (which was not certified by peer review) is the author/funder, who has granted bioRxiv a license to display the preprint in perpetuity. It is made available under a CC-BY 4.0 International license.

cultured post-implantation embryos (**Extended Data Fig. 5a, b**) and then tested the degradation efficiency *in vivo*. To minimize the impact of EED depletion on the pregnant mice, *Eed*$^{dTAG/+}$ female mice were used to mate with *Eed*$^{dTAG/dTAG}$ male mice, and subjected to intraperitoneal (I.P.) injection of dTAG^{V}-1 at E6.0. The embryos were collected for further analyses at E6.5 (**Fig. 5a**) with the *Eed*$^{dTAG/+}$ embryos in the same litter served as a control. The dTAG^{V}-1 is a small molecule that activates the dTAG system vial the VHL degradation pathway and has been shown to have low toxicity and high efficiency for *in vivo* degradation [34]. Immunostaining analyses indicated that both EED and H3K27me3 were near completely depleted after ~12-hr dTAG^{V}-1 treatment (**Fig. 5a**). Similarly, administration of dTAG^{V}-1 at E6.5 also led to near complete degradation of both EED and H3K27me3 by E7.5 (**Fig. 5a**). Thus, the Eed-dTAG system allows efficient and inducible degradation of PRC2 in early post-implantation embryos *in vivo*.

We then dissected E6.5 EPI, ExE and visceral endoderm (VE) from *Eed*$^{dTAG/+}$ and *Eed*$^{dTAG/dTAG}$ embryos for RNA-seq analyses (**Extended Data Fig. 5c**). Unexpectedly, acute EED depletion had limited impact on EPI and VE transcriptomes (**Extended Data Fig. 5d and Supplementary Table 5**). However, more genes, including bivalent genes (52 out of 284) are up-regulated (FC>2, adjusted p<0.05) in ExE lineage after EED degradation (**Fig. 5b, c, Extended Data Fig. 5e and Supplementary Table 5**). Further analysis showed that the global bivalent gene expression is increased with EED degradation (**Extended Data Fig. 5f and Supplementary Table 4**). The GO terms enriched in the up-regulated genes in EED-depleted E6.5 ExE include developmental processes such as “ossification” and “mesenchyme development” (**Extended Data Fig. 5g**), suggesting PRC2 also repress development genes in ExE lineage. These results indicate that PRC2 is necessary for silencing bivalent genes and development genes in the ExE lineage.

Given that the ExE lineage derived BMP4 is essential for PGC induction in a dosage-dependent manner [44-46], and that loss of PRC2 lead to overproduction of PGCs (SOX2^{+}/TFAP2C^{+}) (**Fig. 5d, e**) [47], we hypothesized that PRC2-mediated repression of *Bmp4* in the ExE lineage might regulate PGCs specification. Indeed, *Bmp4* mRNA level increased by ~15 fold upon EED depletion in E6.5 ExE, but not in EPI or VE (**Fig. 5f**). To determine whether the increased *Bmp4* level in the ExE is responsible for the expanded PGC fate in EED-depleted embryos (**Fig. 5d, e**), we knocked out *Bmp4* in *Eed*$^{dTAG/dTAG}$ embryos by zygotic CRISPR injection (Methods) and assessed PGCs numbers at E7.5. Remarkably, *Bmp4* KO caused complete loss of PGCs even in EED-depleted embryos (**Fig. 5g, h**). Given that PGCs are derived from the EPI lineage, and the *Bmp4* is upregulated in the ExE lineages in response to EED degradation, these data support that EED restricts PGC numbers in EPI through a lineage crosstalk between ExE and EPI. Interestingly, CUT&RUN analyses showed negligible H3K27me3 enrichment at the *Bmp4* locus (**Fig.**

bioRxiv preprint doi: https://doi.org/10.64898/2026.01.20.700679; this version posted January 20, 2026. The copyright holder for this preprint (which was not certified by peer review) is the author/funder, who has granted bioRxiv a license to display the preprint in perpetuity. It is made available under a CC-BY 4.0 International license.

5i and Extended Data Fig. 5h) indicating that PRC2 represses *Bmp4* in the ExE lineage likely through an indirect mechanism.

PRC2 represses *Bmp4* indirectly through repressing the bivalent gene *Esrrb* in ExE

To investigate how PRC2 activity in ExE may regulate PGCs specification in EPI, we identified a list of transcription factors that are enriched for both H3K27me3 and H3K4me3 marks in E6.5 ExE and are up-regulated upon EED depletion in the same lineage (**Fig. 6a**). Of these candidates, the orphan nuclear receptor *Esrrb* (estrogen related receptor beta), which is expressed only in the ExE lineage at E6.5 embryo, has been shown to induce *Bmp4* expression in E6.5 ExE and is critical for PGC specification[48]. Interestingly, *Esrrb* is a bivalent gene enriched for both H3K4me3 and H3K27me3 in the ExE lineage (**Fig. 6b and Extended Data Fig. 5e**), indicating *Esrrb* is a direct target of PRC2.

To identify downstream targets of *Esrrb*, we acutely knocked out *Esrrb* by zygotic CRISPR injection (Methods) and performed RNA-seq analyses in E6.5 ExE (**Fig. 6c**). Despite that depletion of *Esrrb* did not affect overall embryo morphology at this stage (**Extended Data Fig. 6a**), which is consistent with a previous study[48], transcriptome analyses revealed 672 and 853 genes were respectively up- and down-regulated in *Esrrb* KO E6.5 ExE (**Fig. 6d, Extended Data Fig. 6b and Supplementary Table 6**). Down-regulation of *Esrrb* confirmed the successful KO of *Esrrb* in the embryos analyzed (**Fig. 6e**). The up-regulated genes are enriched for GO terms including "actin filament organization" and "fiber organization", whereas the down-regulated genes are enriched for GO terms such as "mesenchyme development" and "formation of primary germ layer" (**Extended Data Fig. 6c, d**). Interestingly, 139 of the down-regulated genes in *Esrrb* KO were also up-regulated in response to EED depletion (**Fig. 6f and Extended Data Fig. 6e**), indicating that the up-regulated genes in the EED-depleted embryos could be mediated by the de-repression of *Esrrb* (**Fig. 6a, f**). Among these 139 up-regulated genes is *Bmp4*, suggesting that PRC2 may indirectly suppress *Bmp4* and PGC fate by directly repressing *Esrrb.*

To test this hypothesis, we acutely depleted *Esrrb* in $Eed^{dTAG/dTAG}$ embryos by zygotic CRISPR injection (Methods) followed by RNA-seq analyses in E6.5 ExE samples. As expected, upregulation of the 139 genes in the EED-depleted embryos were near completely reversed by *Esrrb* KO (**Fig. 6h**). Notably, the increased *Bmp4* RNA level upon EED depletion was also largely rescued by *Esrrb* KO (**Fig. 6i**). However, this rescue was incomplete, likely because PRC2 may also directly repressed *Bmp4* to some extent (**Fig. 5i**). Nonetheless, we next evaluated to what extent *Esrrb* KO may reverse the expanded PGC phenotype in the EED-depleted embryos (**Fig. 5d, e**). Like *Bmp4* KO (**Fig. 5g, h**), *Esrrb* KO also greatly reduced the PGC numbers in EED-depleted E7.5 embryos (**Fig. 6j, k**). Collectively, these data indicate that PRC2 suppresses

bioRxiv preprint doi: https://doi.org/10.64898/2026.01.20.700679; this version posted January 20, 2026. The copyright holder for this preprint (which was not certified by peer review) is the author/funder, who has granted bioRxiv a license to display the preprint in perpetuity. It is made available under a CC-BY 4.0 International license.

Bmp4 and PGC fate largely through direct repressing *Esrrb* in the ExE lineage, highlight the lineage crosstalk-dependent functions of PRC2 in regulating PGCs formation.

Esrrb regulates its downstream targets primarily by binding to their enhancers

Having demonstrated that *Esrrb* is a direct target of PRC2, and ESRRB promotes PGC fate by activating *Bmp4* signaling (**Fig. 6**), we next sought to understand how ESRRB regulates its downstream target genes at the chromatin level. To this end, we first performed ESRRB CUT&RUN analyses in E6.5 and E7.0 ExE lineage. We found that the two biological replicates are highly similar, and the ESRRB binding profiles at the two developmental stages are largely comparable (**Fig. 7a and Extended Data Fig. 7a**). Further analysis showed that ESRRB co-binding with its co-factor SOX2 (**Extended Data Fig. 7b, c**)[49], which confirm the reliability of ESRRB binding peaks. Detailed analyses of the CUT&RUN datasets revealed that the ESRRB peaks are mostly located at introns and distal intergenic regions, with only a small percentage of peaks found at promoter regions (**Extended Data Fig. 7d**). This observation indicates that ESRRB mainly bind to putative enhancer regions. Indeed, ESRRB bound to well characterized enhancers or super-enhancers of *Bmp4*, *Cdx2,* and *Sox2* (**Fig. 7b**). Importantly, all these genes are downregulated upon *Esrrb* KO in E6.5 ExE samples (**Fig. 7b)**, supporting the notion that ESRRB promotes expression of these genes by activating their enhancers.

Since one hallmark of enhancer is the enrichment of H3K27ac [50], we next investigated how loss of ESRRB may affect H3K27ac at enhancer regions. To this end, we performed H3K27ac CUT&RUN analyses in E6.5 ExE and found that H3K27ac levels at ESRRB-bound distal/intron regions are greatly reduced upon *Esrrb* KO (i.e., *Bmp4*, *Klf9*, *Wnt6*, *Sox21*, *Fbxo21*, **Fig. 7c, d and Extended Data Fig. 7e**). In contrast, the effect of *Esrrb* KO on H3K27ac levels at ESRRB-bound promoters is much milder (i.e., *Rbm47*, **Fig. 7c, d**).

To understand how ESRRB may synergistically activate enhancers with other transcription factors in ExE, we next focused on TFAP2C, a critical TF for ExE development [51,52] with many shared targets with ESRRB (**Fig. 7e**). Interestingly, clustering analyses revealed that a subset of the co-bound peaks exhibited biased enrichment of these two transcription factors (i.e., cluster 1 and cluster 2 in **Fig. 7e**), indicating that these two TFs may have differential preference to different enhancer elements. Interestingly, ESRRB only regulates H3K27ac levels at peaks where it had a stronger enrichment than TFAP2C (**Fig. 7e, f**). It's possible that TFAP2C may compensate the enhancer activity upon ESRRB KO at the peaks with a biased enrichment of TFAP2C. Thus, these data suggest that ESRRB regulates H3K27ac deposition mainly at its

bioRxiv preprint doi: https://doi.org/10.64898/2026.01.20.700679; this version posted January 20, 2026. The copyright holder for this preprint (which was not certified by peer review) is the author/funder, who has granted bioRxiv a license to display the preprint in perpetuity. It is made available under a CC-BY 4.0 International license.

target gene enhancers, but not promoters, in E6.5 ExE. Additionally, at the ESRRB predominate enhancers, ESRRB is critical for gene activation independent of TFAP2C.

Collectively, these data support our notion that PRC2 plays a critical role in restricting PGCs number through a PRC2-ESRRB-BMP4 regulatory axis (**Fig. 7g**), and ESRRB regulates gene expression mainly by modulating enhancer activity (**Fig. 7h**).

bioRxiv preprint doi: https://doi.org/10.64898/2026.01.20.700679; this version posted January 20, 2026. The copyright holder for this preprint (which was not certified by peer review) is the author/funder, who has granted bioRxiv a license to display the preprint in perpetuity. It is made available under a CC-BY 4.0 International license.

Discussion

In this study, we systematically evaluated the function of PRC2 in mouse early embryogenesis by using a rapid protein degradation EED dTAG mouse model. Such targeted protein degradation system has two major advantages compared to conventional zygotic and maternal KOs. First, it enables depletion of maternal EED without using oocyte-specific Cre lines (*i.e., Gdf9-Cre* and *Zp3-Cre*). The germline conditional KO lines activate *Cre* expression at early stage of oogenesis (*i.e.,* postnatal day 3-5)[53] and may cause accumulative compensatory and/or secondary effects in growing oocytes. Indeed, loss of PRC2 results in de-repression of certain Polycomb targets in oocytes, although the phenotypes are much milder than those of the PRC1 conditional KO [26,54,55]. Second, the dTAG system allows for rapid depletion of EED at different developmental stages to reveal stage-specific PRC2 functions, which is not feasible when using conventional KO approaches. Using this novel strategy, we are able to uncover previously underappreciated stage-specific roles of PRC2 in regulating MZT, cell lineage-specification, and bivalency acquisition during pre- and peri-implantation development. We further elucidated the mechanism underlying how PRC2 controls proper PGC numbers through a PRC2-ESRRB-BMP4 regulatory axis and a lineage crosstalk.

Previous zygotic and maternal KOs have demonstrated important functions of PRC2 in early embryogenesis. The key conclusions from these studies are: 1) zygotic PRC2 is required for proper gastrulation, and 2) maternal PRC2 is critical for post-implantation development. Specifically, maternal PRC2 KO using *Gdf9-Cre* or *Zp3-Cre* causes defective imprinted X-chromosome inactivation (XCI), loss of non-canonical imprinting, partial lethality after implantation, and placental hyperplasia [28,29,31-33,41,56]. Importantly, these *Eed* maternal KO-associated defects can be largely rescued by correcting the abnormal XCI and non-canonical imprinting [32,33]. In contrast to the earlier studies emphasizing the roles of PRC2 in post-implantation development, our study revealed a previously not appreciated PRC2 function in regulating pre-implantation development. We showed that PRC2 is required for maintaining the repression of certain Polycomb target genes in late 2-cells, morulae, and ICM of late blastocysts. Depletion of EED results in abnormal gene expression as exemplified by the reduced ICM/TE marker expressions at morula stage, the increased expression of developmental genes, and other lineage markers for all three stages examined. Such ectopic expression likely contributes to the defective first and second cell fate specification at early and late blastocyst stages. It should also be noted that the lineage differentiation defects observed in this work is more severe than the maternal EED or EZH1/2 KO studies [29,56,57], which is likely due to depletion of both maternal and zygotic PRC2 by the dTAG approach.

bioRxiv preprint doi: https://doi.org/10.64898/2026.01.20.700679; this version posted January 20, 2026. The copyright holder for this preprint (which was not certified by peer review) is the author/funder, who has granted bioRxiv a license to display the preprint in perpetuity. It is made available under a CC-BY 4.0 International license.

In addition to revealing the functions of PRC2 in MZT and lineage specifications, our study also uncovered novel insights into bivalency establishment and illustrated how PRC2 regulates bivalency *in vivo*. By mapping H3K27me3 and H3K4me3 dynamics throughout early embryogenesis, we provide strong evidence indicating that bivalency acquisition mainly started in the E4.5 ICM and further increased in E6.5 EPI, which is in contrast to a previous study suggesting that bivalency is largely absent or infrequent in preimplantation embryos but established after implantation [36]. We further revealed the different mechanisms underlying bivalency acquisition in ICM and EPI. In the first wave (*i.e.,* E3.5 to E4.5 ICM), the gain of bivalency is mainly due to the increase in both H3K27me3 and H3K4me3. The increase of H3K27me3 in late blastocysts is likely to be catalyzed by PRC2.2 as deletion of the PRC2.2-specific subunits *Jarid2/Aebp2* abolishes H3K27me2 acquisition in morulae and subsequent H3K27me3 gain in blastocysts [58]. In contrast, H3K27me3 already occupied most of the E6.5 bivalent genes at the E4.5 ICM stage, and the gain of bivalency during the 2nd wave (*i.e.,* E4.5 to E6.5 EPI) is largely due to the increase in H3K4me3. The increase of H3K4me3 in E6.5 EPI might be mediated by the H3K4 methyltransferase KMT2B, which is critical for establishing bivalent H3K4me3 at this stage [59]. In addition, we also showed that acute EED depletion preferentially derepresses bivalent genes with higher H3K4me3, implying that H3K4me3 likely poising these genes for activation.

Previous studies have been mainly focused on how epigenetic factors directly regulate embryonic development [47]. Our study on the role of PRC2 in PGC specification highlights the importance of lineage crosstalk, raising the possibility that epigenetic factors regulate embryogenesis via both cell-autonomous and non-cell-autonomous pathways. We showed that one of the notable direct PRC2 targets in E6.5 ExE is *Esrrb* (a bivalent gene in ExE), a transcription factor implicated in naïve pluripotency [60], formative pluripotency [61], and trophoblast development [62,63]. *Esrrb* null embryos showed reduced numbers of PGCs, which has been credited to lower level of BMP4 from ExE [48]. Through a series of *in vivo* genetic manipulations and epigenome profiling, we demonstrated that PRC2 regulates *Bmp4* expression in ExE through the PRC2-ESRRB-BMP4 regulatory axis that is critical for proper PGC specification in EPI during gastrulation. Specifically, H3K27me3 is critical for controlling the level of *Esrrb* in ExE. *Esrrb* in turn directly induces *Bmp4* expression by activating its distal enhancer, and BMP4 from ExE guides PGC specification in EPI. It should be noted that H3K27me3 does not completely silence *Esrrb* transcription, but rather to prevent it from overexpressing in the ExE lineage. We also revealed that ESRRB regulates its targets largely by activating their enhancers. ESRRB has been shown as a pioneer factor that can induce local DNA hypomethylation, displace nucleosomes and recruit co-factors such as p300 [60]. Consistent with this notion, we observed reduced H3K27ac primarily at distal enhancers, but not promoter regions, of ESRRB target genes in E6.5 ExE.

bioRxiv preprint doi: https://doi.org/10.64898/2026.01.20.700679; this version posted January 20, 2026. The copyright holder for this preprint (which was not certified by peer review) is the author/funder, who has granted bioRxiv a license to display the preprint in perpetuity. It is made available under a CC-BY 4.0 International license.

Acute PRC2 depletion at E6.5 embryos had minimal impact on the transcriptome in EPI but affected the expression of hundreds of genes in ExE. It remains unclear how acute loss of PRC2 causes different responses in these two lineages. It is possible that additional repressive chromatin markers that are specific to E6.5 EPI help maintain Polycomb repression in the absence of PRC2. This possibility raises a question: which epigenetic factors may interplay with PRC2 to silence bivalent genes in E6.5 EPI. PRC1 is one of the potential candidates, since it has also been proposed that H2AK119ub1 could be an important contributor to bivalency during preimplantation development [43]. In addition, inducible PRC1 or PRC2 KO right after implantation suggest that PRC1 and PRC2 are largely independent from each other on the inactive X in extraembryonic tissues[64]. These observations suggest that PRC1/H2AK119ub1 and PRC2/H3K27me3 have different roles in regulating early embryogenesis. Further work is needed to systematically address how PRC1 along or together with PRC2 might regulate MZT, lineage specification, bivalency acquisition and gastrulation.

bioRxiv preprint doi: https://doi.org/10.64898/2026.01.20.700679; this version posted January 20, 2026. The copyright holder for this preprint (which was not certified by peer review) is the author/funder, who has granted bioRxiv a license to display the preprint in perpetuity. It is made available under a CC-BY 4.0 International license.

Methods

Eed$^{dTAG/dTAG}$ mice generation

All experiments were conducted in accordance with the National Institute of Health Guide for Care and Use of Laboratory Animals and were approved by the Institutional Animal Care and Use Committee (IACUC) of Boston Children's Hospital and Harvard Medical School (protocol number IS00000270-9). Mice were housed in specific pathogen-free facilities with regulated temperature (20-22°C) and humidity (40-70%), with a 12-hour light/dark cycle. To generate knock-in mice, the mixture of *Eed* donor DNA (30 ng/μl), sgRNA (40 ng/μl) and Cas9 mRNA (100 ng/μl) were injected into early 2-cell stage embryos with a Piezo-driven micromanipulator (Primer Tech, Ibaraki, Japan). Following injection, embryos were cultured in KSOM medium for 6 hours, and then transferred into the oviducts of pseudo-pregnant ICR female mice (Charles River). The F0 chimeras were backcrossed to C57BL/6J wild-type mice for a minimum of two generations to achieve stable genetic inheritance. The primers used for genotyping are listed in Supplementary Table 7.

Zygotic KO embryo generation

For *Esrrb* and *Bmp4* zygotic KOs, the wide type or *Eed* $^{dTAG/dTAG}$ background 1-cell embryos (6 hpf) were injected with the mixture of sgRNA (20 ng/μl) and Cas9 protein (20 ng/μl). After one day culture, 2-cell embryos were transferred into the oviducts of pseudo-pregnant ICR female mice (Charles River). Post-implantation embryos were collected at E6.5 or E7.0 for further analysis. Small piece of mixture of ExE and VE were used for genotyping. The sgRNAs and primers for genotyping are listed in Supplementary Table 7.

Establishment of *Eed*$^{dTAG/dTAG}$ cell line

Eed$^{dTAG/dTAG}$ ESCs were generated by co-transfecting Eed-HAL-FKBPF36V-V5-HAR donor and px330 (Cas9 and sgRNA) plasmids into ES-E14TG2a cells (ATCC, CRL-1821) and cultured for 24 hours. Then transfected cells were subjected to puromycin selection (Gibco, A1113803) for 48 hours, followed by recovery in puromycin-free medium for 6-7 days. Single clones were picked for genotyping and further experiments. ESCs were maintained on 0.1% gelatin-coated plates under 2i/LIF culture conditions as previous used [65]. The 2i/LIF culture medium consisted of DMEM (Gibco, 11960069) supplemented with 15% fetal bovine serum (Sigma-Aldrich, F6178), 1× MEM non-essential amino acids (Gibco, 11140050), 1 mM sodium pyruvate (Gibco, 11360), 100 U/mL penicillin-streptomycin (Gibco, 15140122), 0.084 mM β-mercaptoethanol (Gibco, 21985023), 2 mM GlutaMAX (Gibco, 35050061), 1000 IU/mL leukemia

bioRxiv preprint doi: https://doi.org/10.64898/2026.01.20.700679; this version posted January 20, 2026. The copyright holder for this preprint (which was not certified by peer review) is the author/funder, who has granted bioRxiv a license to display the preprint in perpetuity. It is made available under a CC-BY 4.0 International license.

inhibitory factor (Millipore, #ESG1107), 0.5 μM PD0325901 (Tocris, 4192), and 3 μM CHIR99021 (Tocris, CHIR99021).

In vitro fertilization and embryo culture

To induce superovulation, wild type C57BL/6J or *Eed*$^{dTAG/dTAG}$ female mice (7-8 weeks old) were injected 7.5 IU of pregnant mare serum gonadotropin (PMSG, BioVendor, RP1782725000), followed by 7.5 IU of human chorionic gonadotropin (hCG, Sigma, C1063) 48 hours later. Oocyte-cumulus complexes (OCCs) were collected 14 hours after hCG injection. Before OCCs collection, sperm was obtained from the cauda epididymis of adult male mice (8-12 weeks old) and capacitated for 40 mins in 200 μl HTF medium (Millipore, MR-070-D). Then OCCs were collected and co-incubated with sperm for 6 hours in HTF medium. Zygotes with two-pronuclear were picked up and transferred to KSOM medium (Millipore, MR-106-D) for further development at 37°C in a humidified 5% CO_2 atmosphere. All the culture medium was covered by mineral oil (Sigma, M5310-1L).

Western blot

1.5×10^6 cells were lysed in 200 μl 1× lysis buffer (50 μl 4 × LDS sample buffer, Invitrogen, NP0007; 20 μl 10 × reducing agent, Invitrogen, NP0007; 2 μl protease inhibitor, sigma, P8340; 128 μl H2O) and incubated on ice for 30 mins. Then the samples were heated at 98 °C for 10 mins, and transferred to ice immediately. 20 μl samples were loaded and run on NuPAGE 4-12% gel (Invitrogen, NP0322BOX), followed by transfer to 0.2 μm PVDF membranes. The primary antibodies anti-EED (1:500, CST, 85322S) and anti-β-actin (1:5000, CST, 4976S) were used for incubation at 4°C overnight. The membranes were washed for three times and incubated with Goat anti-Rabbit IgG (H+L) Superclonal™ Secondary Antibody-HRP (1:2000, Invitrogen, A27036) for 1 hour at room temperature. Target proteins were detected using ECL kit (Thermo Fisher Scientific, 32209) and imaged by iBright1500 (Invitrogen).

Immunostaining and confocal microscope

The same Immunostaining protocol was used for both pre-implantation and post-implantation embryos. Briefly, embryos were fixed in 4% paraformaldehyde/0.5% triton for 20 mins. Following fixation, embryos were washed three times in PBS containing 0.1% Triton X-100 and subsequently blocked in PBS supplemented with 1% bovine serum albumin (BSA) and 0.1% Triton X-100 for 1 h at room temperature. Primary antibody incubations were performed overnight at 4°C using the following dilutions in blocking buffer: anti-EED (1:500, CST, 85322S), anti-H3K27me3 (1:200, Active Motif, 61017), anti-V5 (1:200, Invitrogen, R960-25), anti-OCT4 (1:200, Santa Cruz, sc-5279), anti-GATA4 (1:200, R&D Systems, MAB2606-SP), anti-NANOG (1:200, Abcam, ab80892), anti-CDX2 (1:500, R&D Systems, AF3665-SP),

bioRxiv preprint doi: https://doi.org/10.64898/2026.01.20.700679; this version posted January 20, 2026. The copyright holder for this preprint (which was not certified by peer review) is the author/funder, who has granted bioRxiv a license to display the preprint in perpetuity. It is made available under a CC-BY 4.0 International license.

anti-SOX2 (1:200, R&D Systems, AF2018-SP) and anti-TFAP2C (1:200, Proteintech, 14572-1-AP). After three times of washing, the embryos were incubated with secondary antibodies for 1 hour at room temperature: Donkey anti-Mouse IgG-Alexa Fluor 568 (1:500, Invitrogen, A10037), Donkey anti Rabbit IgG (H+L)-Alexa Fluor 488 (1:500, Invitrogen, A-21206) and Donkey anti-Goat IgG (H+L)-Alexa Fluor 647 (1:500, Invitrogen, A-21447). Hoechst 33342 (10 μg/ml, Sigma) was used for DNA staining. Embryos were imaged with a confocal microscope (Zeiss, LSM800).

Embryo isolation

For E4.5 ICM isolation, E4.5 embryos were treated by Acidic Tyrode's solution (Millipore) to remove the zona pellucida. Embryos were first incubated with anti-mouse serum antibody (1:3 dilution in KSOM medium, Sigma-Aldrich, M5774) for 30 min at 37°C, followed by guinea pig complement (1:3 dilution in KSOM, Millipore, S1639) treatment for 30 min at 37°C. The ICMs were isolated by removing trophectoderm cells with a glass pipette. E4.5 ICM refers to the mixture of EPI and PrE cells. Due to technical difficulties, EPI and PrE cannot be separated. For E6.5 embryo isolation, embryos were dissected from the decidua, followed by removal of the Reichert's membrane. Embryos were then incubated in 100 μl 0.25% trypsin supplemented with 2.5% pancreatin (Sigma, P3292) on ice for 15 minutes. The enzymatic digestion was quenched by adding 100 μl of 10% FBS. The VE layer was manually removed using a glass pipette, the EPI and ExE were isolated using a sharp needle under a dissection microscope.

dTAG treatment

To degrade EED in pre-implantation embryos, *Eed*$^{dTAG/dTAG}$ embryos were cultured in KSOM with 1 μM dTAG13 (Tocris, 6605). To degrade EED in ESCs, *Eed*$^{dTAG/dTAG}$ ESCs were cultured in 2i/LIF medium with 0.5 μM dTAG13. For EED degradation in post-implantation embryos *in vitro*, *Eed*$^{dTAG/dTAG}$ embryos were maintained in culture medium (75% pregnant rat serum, 2 mM GlutaMAX, 11 mM HEPES and 1x MEM NEAA) containing 2 μM dTAG^{V}-1. For EED degradation in post-implantation embryos *in vivo*, intraperitoneal (IP) injections were performed. Specifically, 1 mg dTAG^{V}-1 was initially dissolved in 25 μl DMSO and subsequently diluted with 475 μl 10% castor oil (Sigma, C5135) to prepare the injection solution. Mice (~28 g each) were injected with 1 mg dTAG^{V}-1 every 12 hours to maintain sustained EED degradation.

CUT&RUN, ATAC-seq and RNA-seq libraries preparation and sequencing

CUT&RUN was performed as previously described [65]. Briefly, intact or isolated embryos were mixed with activated Concanavalin A Magnetic Beads (Polysciences, 86057-3) for 10 mins at RT, followed by incubation with primary antibodies overnight at 4°C. After three washes, samples were included with 3

bioRxiv preprint doi: https://doi.org/10.64898/2026.01.20.700679; this version posted January 20, 2026. The copyright holder for this preprint (which was not certified by peer review) is the author/funder, who has granted bioRxiv a license to display the preprint in perpetuity. It is made available under a CC-BY 4.0 International license.

ng/μl pA-MNase (home-made) for 2 hours with rotation at 4 °C. Subsequently, pA-MNase was activated by incubating with 200 μl pre-cooled 0.5 μM $CaCl_2$ for 20 mins at 4 °C, and quench by adding 23 μl 10×stop buffer. To release DNA, samples were first incubated at 37 °C for 15 minutes, followed by addition 2.5 μl 10% SDS and 2.5 μl Proteinase K (20 mg/ml; Thermo Fisher, AM2546), and then incubated at 55 °C for 1 hour. DNA was subsequently purified using phenol-chloroform extraction. DNA library was constructed using NEBNext Ultra II DNA library preparation kit (New England Biolabs, E7645S). Primary antibodies anti-H3K4me3 (1:100, CST, 9727S), anti-H3K27me3 (1:100, Diagenode, C15410069), anti-H2AK119ub1 (1:100, CST, 8240S), and anti-ESRRB (1:100, Proteintech, 22644-1-AP) were used for CUT&RUN.

ATAC-seq was performed as previously described[66]. Briefly, isolated embryos were incubated with Tn5 (Diagenode, C01070012-30) for 15 mins at 37°C. Subsequently, DNA fragments were released by dissecting with Proteinase overnight at 55°C. DNA libraries were constructed with NEBNext High-Fidelity 2×PCR Master Mix (NEB, M0541S).

For RNA-seq, intact or isolated embryos were collected and immediately frozen at -80 °C until use. SMART-Seq™ v4 Kit (Clontech, 634890) was used to construct cDNA libraries, and Nextera® XT DNA Sample Preparation Kit kit (Illumina, FC-131-1024) was used for the sequence libraries construction. All libraries were sequenced by the Illumina NextSeq 1000/2000 system.

RNA-seq data analysis

The raw paired-end sequencing reads of RNA-seq were first processed with the Trimmomatic (v0.39)[67] to remove sequencing adaptors if present. After adaptor trimming, reads with length less than 35 bp were discarded. The trimmed reads were mapped to GRCm38 mouse reference genome using STAR (v2.7.8a)[68]. The gene annotations were downloaded from GENCODE (https://www.gencodegenes.org) with version vM24. The read counts mapped to each gene were calculated using RSEM (v1.3.1)[69] with the transcriptome alignments generated by STAR as input. To calculate differentially expressed genes (DEGs) between conditions, R package DESeq2 (v1.46.0)[70] was used. Genes with adjusted p-value < 0.05, fold change ≥ 2 and mean FPKM ≥ 1 were identified as DEGs. The Gene Ontology (GO) enrichment of DEGs was calculated with R package clusterProfiler (v4.14.3)[71].

CUT&RUN data analysis

The raw paired-end reads of CUT&RUN were trimmed with Trimmomatic (v0.39)[67] to remove sequencing adaptors and the trimmed reads with length at least 35 bp were kept. The cleaned reads were mapped to GRCm38 mouse reference genome using bowtie2 (v2.4.2)[72] with parameters: --local --very-sensitive-local

bioRxiv preprint doi: https://doi.org/10.64898/2026.01.20.700679; this version posted January 20, 2026. The copyright holder for this preprint (which was not certified by peer review) is the author/funder, who has granted bioRxiv a license to display the preprint in perpetuity. It is made available under a CC-BY 4.0 International license.

--no-unal --no-mixed --no-discordant --dovetail -I 10 -X 700 --soft-clipped-unmapped-tlen. Picard MarkDuplicates (v2.23.4) were used to remove PCR duplicates. The aligned reads were further filtered to retain proper paired reads with a minimum mapping quality of 30. For histone modifications CUT&RUN data, the FPKM (fragments per kilobase region per million mapped fragments) signal tracks were generated with bamCoverage in deeptools (v3.5.1)[73] with 100 bp bin size. For TF CUT&RUN data, the CPM (counts per million) signal tracks were generated with bamCoverage in deeptools (v3.5.1) with 1 bp bin size. To call peaks for H3K4me3 ChIP-seq data and ESRRB CUT&RUN data, the MACS2 (v2.2.7.1)[74] was used with parameters: -f BAMPE -B --SPMR -p 1e-4 -g mm. The reproducible peaks between two replicates were calculated with the irreproducible discovery rate (IDR) framework[75], with the IDR cutoff of 0.05. For ESRRB binding peaks, we further filtered them with q-value cutoff of 10^{-30} to remove weak binding peaks. The heatmaps of CUT&RUN signals around TSSs or peak centers were calculated with computeMatrix in deeptools (v3.5.1) with bin sizes of 10, and plotted with R packages profileplyr (v1.22.0) and EnrichedHeatmap (v1.36.0). The promoter (±1 kb around TSS) average levels of H3K27me3 or H3K4me3 were calculated with multiBigwigSummary in deeptools (v3.5.1). For genes with multiple TSSs, the highest value among all the TSSs was used as the signal level of that gene.

ATAC-seq data analysis

The signal tracks of ATAC–seq were calculated with the ENCODE ATAC–seq pipeline using default parameters (v2.1.2, https://github.com/ENCODE-DCC/atac-seq-pipeline), and the fold change signal tracks were used.

Histone modification signal normalization across stages

To study the H3K27me3 or H3K4me3 levels across different developmental stages, the FPKM values need to be normalized to make them comparable. We used a normalization method as previously described[76,77]. Briefly, we first calculated the average FPKM at gene promoter regions (-1,000 bp to +500 bp around TSS) and ranked them in descending order. For each stage, the median FPKM value of the top 3,000 promoters were considered as the saturated signal value of that stage. Then the saturated value of each stage was divided by the saturated value of ESC (or ICM) stage to get the scale factor for that stage. Finally for each stage, the original FPKM values were multiplied by the scale factor of that stage to obtain the normalized FPKM.

Bivalent gene identification

Bivalent genes were identified based on the normalized FPKM of H3K27me3 and H3K4me3 at promoter regions. For all the stages, genes with both signal values above a unified threshold were considered as

bioRxiv preprint doi: https://doi.org/10.64898/2026.01.20.700679; this version posted January 20, 2026. The copyright holder for this preprint (which was not certified by peer review) is the author/funder, who has granted bioRxiv a license to display the preprint in perpetuity. It is made available under a CC-BY 4.0 International license.

bivalent genes. To find the threshold, we used the number of overlapped peaks between H3K4me3 and H3K27me3 in E4.5 ICM as a reference. Specifically, the H3K4me3 peaks in E4.5 ICM were called as described above. The average raw FPKM of H3K27me3 at these regions (±2 kb around H3K4me3 peak center) was calculated and regions with a value ≥ 3 were considered as strong H3K27me3 domains overlapping with H3K4me3 peaks, which resulted in 1,457 such bivalent regions in E4.5 ICM. Then we searched a threshold value θ (θ = 6.365) so that when the genes promoter normalized FPKM of H3K27me3 ≥ θ and the normalized FPKM of H3K4me3 ≥ θ in E4.5 ICM, the same number (1,457) of regions could be derived. Finally, for each stage, genes with promoter normalized FPKM of H3K27me3 ≥ 6.365 and the normalized FPKM of H3K4me3 ≥ 6.365 were identified as bivalent genes of that stage.

Public data sets used

RNA-seq of mouse pre-implantation embryos[78,79]: GSE71434 and GSE76505. Ribo-seq of mouse pre-implantation embryos[37]: GSE169632. H3K27me3 ChIP-seq of mouse pre-implantation embryos[40]: GSE73952. H3K4me3 ChIP-seq of mouse pre-implantation embryos[78]: GSE71434. H3K4me3 ChIP-seq of mouse post-implantation embryos[59,80]: GSE125318 and GSE124212. TFAP2C and SOX2 CUT&RUN of E6.5 ExE embryos[81]: GSE216256.

bioRxiv preprint doi: https://doi.org/10.64898/2026.01.20.700679; this version posted January 20, 2026. The copyright holder for this preprint (which was not certified by peer review) is the author/funder, who has granted bioRxiv a license to display the preprint in perpetuity. It is made available under a CC-BY 4.0 International license.

References

1. Kojima, M.L., Hoppe, C. & Giraldez, A.J. The maternal-to-zygotic transition: reprogramming of the cytoplasm and nucleus. *Nat Rev Genet* **26**, 245-267 (2025).

2. Jukam, D., Shariati, S.A.M. & Skotheim, J.M. Zygotic Genome Activation in Vertebrates. *Dev Cell* **42**, 316-332 (2017).

3. Schulz, K.N. & Harrison, M.M. Mechanisms regulating zygotic genome activation. *Nat Rev Genet* **20**, 221-234 (2019).

4. Kravchenko, P. & Tachibana, K. Rise and SINE: roles of transcription factors and retrotransposons in zygotic genome activation. *Nat Rev Mol Cell Biol* **26**, 68-79 (2025).

5. Zou, Z., Wang, Q., Wu, X., Schultz, R.M. & Xie, W. Kick-starting the zygotic genome: licensors, specifiers, and beyond. *EMBO Rep* **25**, 4113-4130 (2024).

6. Zernicka-Goetz, M., Morris, S.A. & Bruce, A.W. Making a firm decision: multifaceted regulation of cell fate in the early mouse embryo. *Nat Rev Genet* **10**, 467-77 (2009).

7. Chen, Q., Shi, J., Tao, Y. & Zernicka-Goetz, M. Tracing the origin of heterogeneity and symmetry breaking in the early mammalian embryo. *Nat Commun* **9**, 1819 (2018).

8. Rossant, J. Genetic Control of Early Cell Lineages in the Mammalian Embryo. *Annu Rev Genet* **52**, 185-201 (2018).

9. Wen, D. & Wang, J. Totipotency or plenipotency: rethinking stem cell bipotentiality. *Curr Opin Genet Dev* **92**, 102342 (2025).

10. Pera, M.F. & Rossant, J. The exploration of pluripotency space: Charting cell state transitions in peri-implantation development. *Cell Stem Cell* **28**, 1896-1906 (2021).

11. Smith, A. Formative pluripotency: the executive phase in a developmental continuum. *Development* **144**, 365-373 (2017).

12. Magnusdottir, E. & Surani, M.A. How to make a primordial germ cell. *Development* **141**, 245-52 (2014).

13. Piunti, A. & Shilatifard, A. The roles of Polycomb repressive complexes in mammalian development and cancer. *Nat Rev Mol Cell Biol* **22**, 326-345 (2021).

14. Blackledge, N.P. & Klose, R.J. The molecular principles of gene regulation by Polycomb repressive complexes. *Nat Rev Mol Cell Biol* **22**, 815-833 (2021).

bioRxiv preprint doi: https://doi.org/10.64898/2026.01.20.700679; this version posted January 20, 2026. The copyright holder for this preprint (which was not certified by peer review) is the author/funder, who has granted bioRxiv a license to display the preprint in perpetuity. It is made available under a CC-BY 4.0 International license.

15. Kim, J.J. & Kingston, R.E. Context-specific Polycomb mechanisms in development. *Nat Rev Genet* **23**, 680-695 (2022).

16. Tamburri, S., Rustichelli, S., Amato, S. & Pasini, D. Navigating the complexity of Polycomb repression: Enzymatic cores and regulatory modules. *Mol Cell* **84**, 3381-3405 (2024).

17. Wang, H. *et al.* Role of histone H2A ubiquitination in Polycomb silencing. *Nature* **431**, 873-8 (2004).

18. de Napoles, M. *et al.* Polycomb group proteins Ring1A/B link ubiquitylation of histone H2A to heritable gene silencing and X inactivation. *Dev Cell* **7**, 663-76 (2004).

19. Cao, R. *et al.* Role of histone H3 lysine 27 methylation in Polycomb-group silencing. *Science* **298**, 1039-43 (2002).

20. Margueron, R. & Reinberg, D. The Polycomb complex PRC2 and its mark in life. *Nature* **469**, 343-9 (2011).

21. Muller, J. *et al.* Histone methyltransferase activity of a Drosophila Polycomb group repressor complex. *Cell* **111**, 197-208 (2002).

22. Kuzmichev, A., Nishioka, K., Erdjument-Bromage, H., Tempst, P. & Reinberg, D. Histone methyltransferase activity associated with a human multiprotein complex containing the Enhancer of Zeste protein. *Genes Dev* **16**, 2893-905 (2002).

23. O'Carroll, D. *et al.* The polycomb-group gene Ezh2 is required for early mouse development. *Mol Cell Biol* **21**, 4330-6 (2001).

24. Faust, C., Schumacher, A., Holdener, B. & Magnuson, T. The eed mutation disrupts anterior mesoderm production in mice. *Development* **121**, 273-85 (1995).

25. Pasini, D., Bracken, A.P., Jensen, M.R., Lazzerini Denchi, E. & Helin, K. Suz12 is essential for mouse development and for EZH2 histone methyltransferase activity. *EMBO J* **23**, 4061-71 (2004).

26. Jarred, E.G. *et al.* Transient Polycomb activity represses developmental genes in growing oocytes. *Clin Epigenetics* **14**, 183 (2022).

27. Chen, Z. & Zhang, Y. Maternal H3K27me3-dependent autosomal and X chromosome imprinting. *Nat Rev Genet* **21**, 555-571 (2020).

28. Chen, Z., Yin, Q., Inoue, A., Zhang, C. & Zhang, Y. Allelic H3K27me3 to allelic DNA methylation switch maintains noncanonical imprinting in extraembryonic cells. *Sci Adv* **5**, eaay7246 (2019).

bioRxiv preprint doi: https://doi.org/10.64898/2026.01.20.700679; this version posted January 20, 2026. The copyright holder for this preprint (which was not certified by peer review) is the author/funder, who has granted bioRxiv a license to display the preprint in perpetuity. It is made available under a CC-BY 4.0 International license.

29. Inoue, A., Chen, Z., Yin, Q. & Zhang, Y. Maternal Eed knockout causes loss of H3K27me3 imprinting and random X inactivation in the extraembryonic cells. *Genes Dev* **32**, 1525-1536 (2018).

30. Harris, C. *et al.* Conversion of random X-inactivation to imprinted X-inactivation by maternal PRC2. *Elife* **8**(2019).

31. Oberin, R. *et al.* Fetal growth delay caused by loss of non-canonical imprinting is resolved late in pregnancy and culminates in offspring overgrowth. *Elife* **13**(2024).

32. Matoba, S. *et al.* Noncanonical imprinting sustains embryonic development and restrains placental overgrowth. *Genes Dev* **36**, 483-494 (2022).

33. Inoue, A. Noncanonical imprinting: intergenerational epigenetic inheritance mediated by Polycomb complexes. *Curr Opin Genet Dev* **78**, 102015 (2023).

34. Nabet, B. *et al.* Rapid and direct control of target protein levels with VHL-recruiting dTAG molecules. *Nat Commun* **11**, 4687 (2020).

35. Nabet, B. *et al.* The dTAG system for immediate and target-specific protein degradation. *Nat Chem Biol* **14**, 431-441 (2018).

36. Zheng, H. *et al.* Resetting Epigenetic Memory by Reprogramming of Histone Modifications in Mammals. *Mol Cell* **63**, 1066-79 (2016).

37. Zhang, C., Wang, M., Li, Y. & Zhang, Y. Profiling and functional characterization of maternal mRNA translation during mouse maternal-to-zygotic transition. *Sci Adv* **8**, eabj3967 (2022).

38. Zhang, M., Wang, F., Kou, Z., Zhang, Y. & Gao, S. Defective chromatin structure in somatic cell cloned mouse embryos. *J Biol Chem* **284**, 24981-7 (2009).

39. Gu, B., Posfai, E. & Rossant, J. Efficient generation of targeted large insertions by microinjection into two-cell-stage mouse embryos. *Nat Biotechnol* **36**, 632-637 (2018).

40. Liu, X. *et al.* Distinct features of H3K4me3 and H3K27me3 chromatin domains in pre-implantation embryos. *Nature* **537**, 558-562 (2016).

41. Inoue, A., Jiang, L., Lu, F., Suzuki, T. & Zhang, Y. Maternal H3K27me3 controls DNA methylation-independent imprinting. *Nature* **547**, 419-424 (2017).

42. Chen, Z., Djekidel, M.N. & Zhang, Y. Distinct dynamics and functions of H2AK119ub1 and H3K27me3 in mouse preimplantation embryos. *Nat Genet* **53**, 551-563 (2021).

bioRxiv preprint doi: https://doi.org/10.64898/2026.01.20.700679; this version posted January 20, 2026. The copyright holder for this preprint (which was not certified by peer review) is the author/funder, who has granted bioRxiv a license to display the preprint in perpetuity. It is made available under a CC-BY 4.0 International license.

731 43. Macrae, T.A., Fothergill-Robinson, J. & Ramalho-Santos, M. Regulation, functions and
732 transmission of bivalent chromatin during mammalian development. *Nat Rev Mol Cell Biol* **24**, 6-
733 26 (2023).

734 44. Lawson, K.A. *et al.* Bmp4 is required for the generation of primordial germ cells in the mouse
735 embryo. *Genes Dev* **13**, 424-36 (1999).

736 45. Ohinata, Y. *et al.* A signaling principle for the specification of the germ cell lineage in mice. *Cell*
737 **137**, 571-84 (2009).

738 46. Hadas, R. *et al.* Temporal BMP4 effects on mouse embryonic and extraembryonic development.
739 *Nature* **634**, 652-661 (2024).

740 47. Grosswendt, S. *et al.* Epigenetic regulator function through mouse gastrulation. *Nature* **584**, 102-
741 108 (2020).

742 48. Okamura, E. *et al.* Esrrb function is required for proper primordial germ cell development in
743 presomite stage mouse embryos. *Dev Biol* **455**, 382-392 (2019).

744 49. Hutchins, A.P. *et al.* Co-motif discovery identifies an Esrrb-Sox2-DNA ternary complex as a
745 mediator of transcriptional differences between mouse embryonic and epiblast stem cells. *Stem*
746 *Cells* **31**, 269-81 (2013).

747 50. Calo, E. & Wysocka, J. Modification of enhancer chromatin: what, how, and why? *Mol Cell* **49**,
748 825-37 (2013).

749 51. Werling, U. & Schorle, H. Transcription factor gene AP-2 gamma essential for early murine
750 development. *Mol Cell Biol* **22**, 3149-56 (2002).

751 52. Auman, H.J. *et al.* Transcription factor AP-2gamma is essential in the extra-embryonic lineages
752 for early postimplantation development. *Development* **129**, 2733-47 (2002).

753 53. Lan, Z.J., Xu, X. & Cooney, A.J. Differential oocyte-specific expression of Cre recombinase
754 activity in GDF-9-iCre, Zp3cre, and Msx2Cre transgenic mice. *Biol Reprod* **71**, 1469-74 (2004).

755 54. Posfai, E. *et al.* Polycomb function during oogenesis is required for mouse embryonic
756 development. *Genes Dev* **26**, 920-32 (2012).

757 55. Mei, H. *et al.* H2AK119ub1 guides maternal inheritance and zygotic deposition of H3K27me3 in
758 mouse embryos. *Nat Genet* **53**, 539-550 (2021).

759 56. Zhao, Y. *et al.* Maternal Ezh1/2 deficiency in oocyte delays H3K27me2/3 restoration and impairs
760 epiblast development responsible for embryonic sub-lethality in mouse. *Development* **149**(2022).

bioRxiv preprint doi: https://doi.org/10.64898/2026.01.20.700679; this version posted January 20, 2026. The copyright holder for this preprint (which was not certified by peer review) is the author/funder, who has granted bioRxiv a license to display the preprint in perpetuity. It is made available under a CC-BY 4.0 International license.

57. Prokopuk, L. *et al.* Loss of maternal EED results in postnatal overgrowth. *Clin Epigenetics* **10**, 95 (2018).

58. Matsuwaka, M., Kumon, M. & Inoue, A. H3K27 dimethylation dynamics reveal stepwise establishment of facultative heterochromatin in early mouse embryos. *Nat Cell Biol* **27**, 28-38 (2025).

59. Xiang, Y. *et al.* Epigenomic analysis of gastrulation identifies a unique chromatin state for primed pluripotency. *Nat Genet* **52**, 95-105 (2020).

60. Adachi, K. *et al.* Esrrb Unlocks Silenced Enhancers for Reprogramming to Naive Pluripotency. *Cell Stem Cell* **23**, 900-904 (2018).

61. Carbognin, E. *et al.* Esrrb guides naive pluripotent cells through the formative transcriptional programme. *Nat Cell Biol* **25**, 643-657 (2023).

62. Gao, H. *et al.* Esrrb plays important roles in maintaining self-renewal of trophoblast stem cells (TSCs) and reprogramming somatic cells to induced TSCs. *J Mol Cell Biol* **11**, 463-473 (2019).

63. Latos, P.A. *et al.* Fgf and Esrrb integrate epigenetic and transcriptional networks that regulate self-renewal of trophoblast stem cells. *Nat Commun* **6**, 7776 (2015).

64. Masui, O. *et al.* Polycomb repressive complexes 1 and 2 are each essential for maintenance of X inactivation in extra-embryonic lineages. *Nat Cell Biol* **25**, 134-144 (2023).

65. Zhou, C., Wang, M., Zhang, C. & Zhang, Y. The transcription factor GABPA is a master regulator of naive pluripotency. *Nat Cell Biol* **27**, 48-58 (2025).

66. Zhang, C. *et al.* The chromatin remodeler Snf2h is essential for oocyte meiotic cell cycle progression. *Genes Dev* **34**, 166-178 (2020).

67. Bolger, A.M., Lohse, M. & Usadel, B. Trimmomatic: a flexible trimmer for Illumina sequence data. *Bioinformatics* **30**, 2114-20 (2014).

68. Dobin, A. *et al.* STAR: ultrafast universal RNA-seq aligner. *Bioinformatics* **29**, 15-21 (2013).

69. Li, B. & Dewey, C.N. RSEM: accurate transcript quantification from RNA-Seq data with or without a reference genome. *BMC Bioinformatics* **12**, 323 (2011).

70. Love, M.I., Huber, W. & Anders, S. Moderated estimation of fold change and dispersion for RNA-seq data with DESeq2. *Genome Biol* **15**, 550 (2014).

71. Yu, G., Wang, L.G., Han, Y. & He, Q.Y. clusterProfiler: an R package for comparing biological themes among gene clusters. *OMICS* **16**, 284-7 (2012).

bioRxiv preprint doi: https://doi.org/10.64898/2026.01.20.700679; this version posted January 20, 2026. The copyright holder for this preprint (which was not certified by peer review) is the author/funder, who has granted bioRxiv a license to display the preprint in perpetuity. It is made available under a CC-BY 4.0 International license.

72. Langmead, B. & Salzberg, S.L. Fast gapped-read alignment with Bowtie 2. *Nat Methods* **9**, 357-9 (2012).

73. Ramirez, F. *et al.* deepTools2: a next generation web server for deep-sequencing data analysis. *Nucleic Acids Res* **44**, W160-5 (2016).

74. Zhang, Y. *et al.* Model-based analysis of ChIP-Seq (MACS). *Genome Biol* **9**, R137 (2008).

75. Landt, S.G. *et al.* ChIP-seq guidelines and practices of the ENCODE and modENCODE consortia. *Genome Res* **22**, 1813-31 (2012).

76. Dahl, J.A. *et al.* Broad histone H3K4me3 domains in mouse oocytes modulate maternal-to-zygotic transition. *Nature* **537**, 548-552 (2016).

77. Wang, M., Chen, Z. & Zhang, Y. CBP/p300 and HDAC activities regulate H3K27 acetylation dynamics and zygotic genome activation in mouse preimplantation embryos. *EMBO J* **41**, e112012 (2022).

78. Zhang, B. *et al.* Allelic reprogramming of the histone modification H3K4me3 in early mammalian development. *Nature* **537**, 553-557 (2016).

79. Zhang, Y. *et al.* Dynamic epigenomic landscapes during early lineage specification in mouse embryos. *Nat Genet* **50**, 96-105 (2018).

80. Hanna, C.W. *et al.* Endogenous retroviral insertions drive non-canonical imprinting in extra-embryonic tissues. *Genome Biol* **20**, 225 (2019).

81. Li, L. *et al.* Lineage regulators TFAP2C and NR5A2 function as bipotency activators in totipotent embryos. *Nat Struct Mol Biol* (2024).

bioRxiv preprint doi: https://doi.org/10.64898/2026.01.20.700679; this version posted January 20, 2026. The copyright holder for this preprint (which was not certified by peer review) is the author/funder, who has granted bioRxiv a license to display the preprint in perpetuity. It is made available under a CC-BY 4.0 International license.

Acknowledgements

We thank Drs. Qianying Yang, Yota Hagihara, Shan Jiang and Boyan Wang for their valuable discussions on the project and comments on the manuscript. This project was supported by NIH (R01HD116750) and the HHMI. Y.Z. is an investigator of the Howard Hughes Medical Institute. Z.C. is supported by the Trustee award from Cincinnati Children's Hospital Medical Center and NIH (R00HD104902). This article is subject to HHMI's Open Access to Publications policy. HHMI lab heads have previously granted a nonexclusive CC BY 4.0 license to the public and a sublicensable license to HHMI in their research articles. Pursuant to those licenses, the author-accepted manuscript of this article can be made freely available under a CC BY 4.0 license immediately upon publication.

Author contributions

Y.Z. conceived and supervised the project. C.Z. and Z.C. design the experiments. C.Z. performed all the experiments. M.W. performed all the bioinformatic analysis. Z.C., C.Z., M.W. and Y.Z. wrote the manuscript. All authors interpreted the data and reviewed the manuscript.

Competing interests

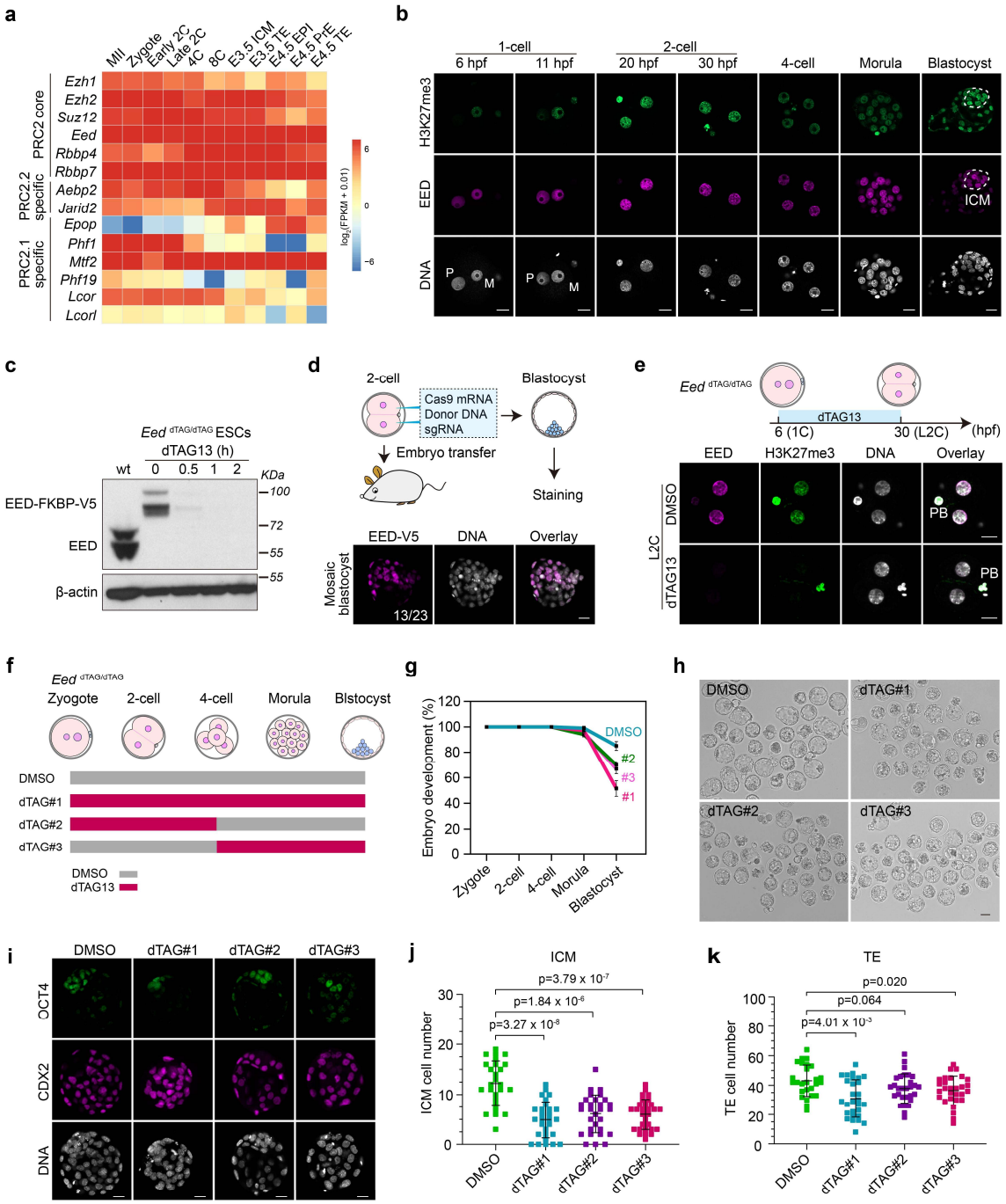
The authors declare no competing interests.

Data and materials availability

All data generated in this study have been deposited to the NCBI Gene Expression Omnibus (GEO) with accession number GSE298615.

bioRxiv preprint doi: https://doi.org/10.64898/2026.01.20.700679; this version posted January 20, 2026. The copyright holder for this preprint (which was not certified by peer review) is the author/funder, who has granted bioRxiv a license to display the preprint in perpetuity. It is made available under a CC-BY 4.0 International license.

Fig. 1



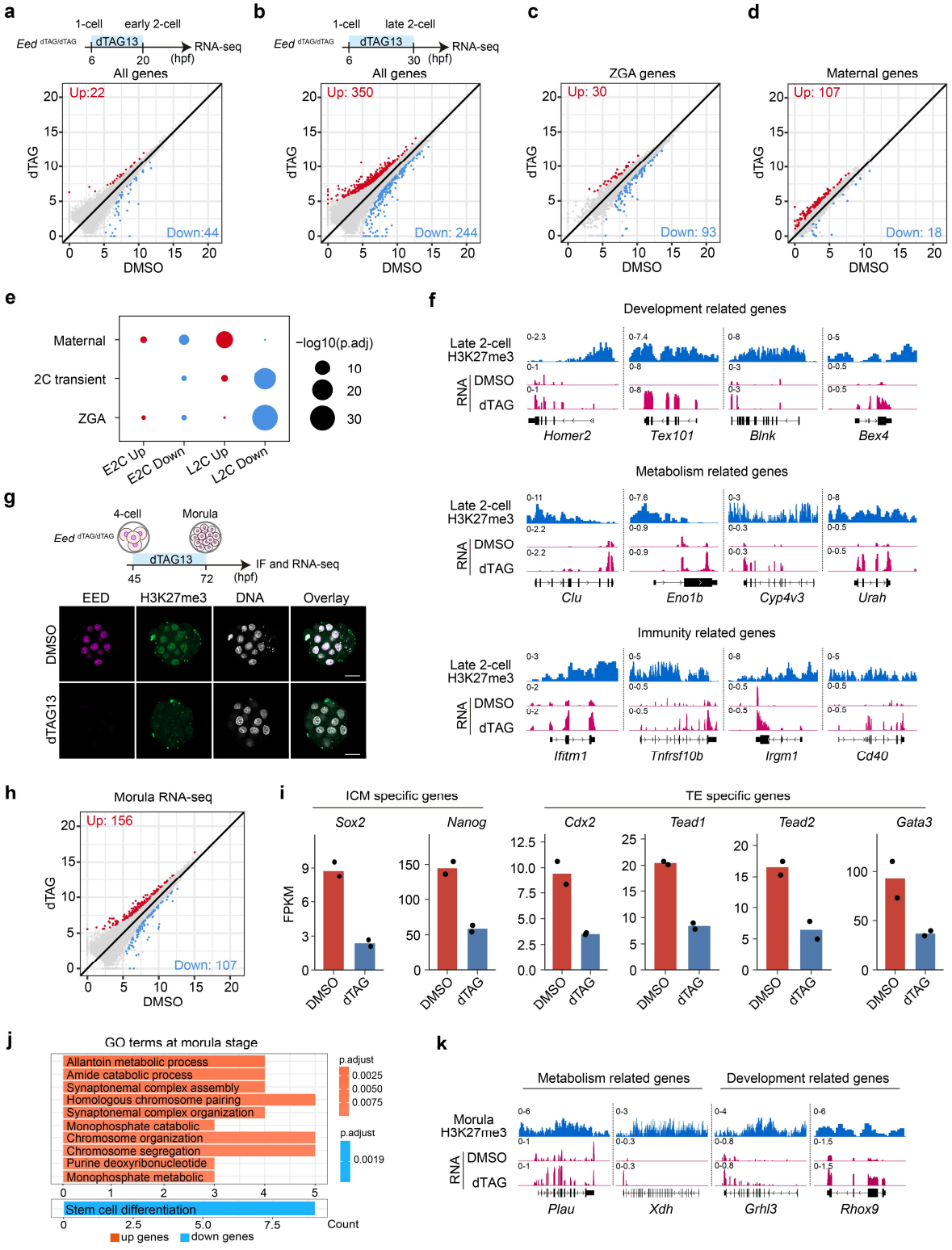
bioRxiv preprint doi: https://doi.org/10.64898/2026.01.20.700679; this version posted January 20, 2026. The copyright holder for this preprint (which was not certified by peer review) is the author/funder, who has granted bioRxiv a license to display the preprint in perpetuity. It is made available under a CC-BY 4.0 International license.

Figure 1. Targeted protein degradation reveals that PRC2 regulates preimplantation development

(**a**) RNA expression dynamics of PRC2 core and accessory subunits during pre- and peri-implantation development. MII: metaphase II eggs; 2C: 2-cell; 4C: 4-cell; 8C: 8-cell; ICM: inner cell mass; TE: trophectoderm; EPI: epiblast; PrE: primitive endoderm; E: embryonic day; FPKM: fragments per kilobase per million mapped reads. (**b**) Immunostaining images showing the dynamics of EED and H3K27me3 during preimplantation development. M: maternal pronuclei; P: paternal pronuclei; hpf: hours post fertilization. The dashed circles indicate the ICM. DNA, Hoechst 33342. Scale bar, 20 μm. (**c**) Immunoblotting images showing the rapid degradation of EED-dTAG protein after dTAG13 treatment in mouse embryonic stem cells. The blots were incubated with anti-EED. β-Actin was used as a loading control. (**d**) Generation of the EED-dTAG mouse model. Top panel: schematic of the two-cell homologous recombination (2C-HR)-CRISPR method; bottom panel: immunostaining of V5 tag of the injected embryos at blastocyst stage. The number of injected embryos showing positive V5 signals were shown. DNA, Hoechst 33342. Scale bar, 20 μm. (**e**) Immunostaining images showing the rapid depletion of EED and H3K27me3 in late 2-cell embryos after dTAG13 treatment starting from zygotes. PB, polar body. DNA, Hoechst 33342. Scale bar, 20 μm. (**f**) Schematic showing the dTAG13 treatment strategies during preimplantation development. (**g**) Percentage of embryos that reach the indicated developmental stages in DMSO and dTAG groups (DMSO, $n = 84$; #1, $n = 69$; #2, $n = 84$; #3, $n = 73$; n represents the total embryos from three independent experiments). The 2-cell, 4-cell, morula, and blastocyst were evaluated at 28, 48, 72, and 96 hrs post fertilization, respectively. The data are presented as mean values ± standard deviation. (**h**) Bright field images showing the embryos in DMSO and dTAG groups at blastocyst stage. (**i**) Immunostaining images showing the ICM ($OCT4^{+}$/ $CDX2^{-}$) and TE ($CDX2^{+}$) cells at blastocyst stage in DMSO and dTAG groups. DNA, Hoechst 33342. Scale bar, 20 μm. (**j-k**) Quantifications of ICM (panel j) and TE (panel k) cells of panel i (DMSO, n=26; #1, n=28; #2, n=29; #3, n=29). *p* values were calculated with Student's *t*-test (two-sided). Experiments were repeated three times.

bioRxiv preprint doi: https://doi.org/10.64898/2026.01.20.700679; this version posted January 20, 2026. The copyright holder for this preprint (which was not certified by peer review) is the author/funder, who has granted bioRxiv a license to display the preprint in perpetuity. It is made available under a CC-BY 4.0 International license.

877 **Fig. 2**



878

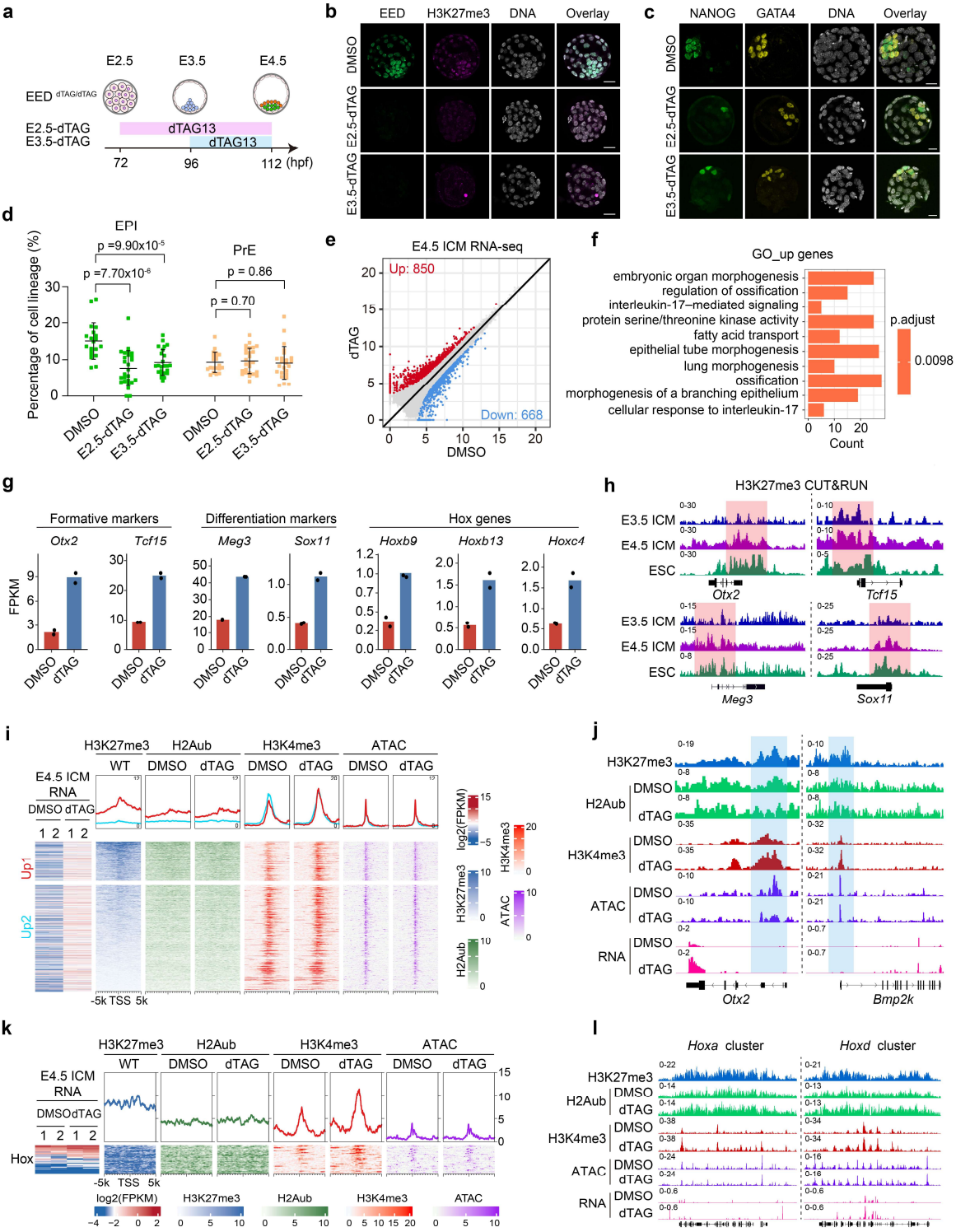
bioRxiv preprint doi: https://doi.org/10.64898/2026.01.20.700679; this version posted January 20, 2026. The copyright holder for this preprint (which was not certified by peer review) is the author/funder, who has granted bioRxiv a license to display the preprint in perpetuity. It is made available under a CC-BY 4.0 International license.

Figure 2. Effects of EED rapid depletion on maternal-to-zygotic transition and mid-preimplantation development

(**a-b**) Scatter plots comparing gene expression changes between DMSO and dTAG groups at early 2-cell (a) and late 2-cell (b) stages. Red and blue dots represent up- and down-regulated genes in the dTAG group, respectively. The cutoff used to define differentially expressed genes: fold change (FC) >= 2, adjusted *p*-value < 0.05, and FPKM >= 1. (**c-d**) Scatter plots comparing expression changes of the major ZGA genes (c) and the maternal genes (d) between DMSO and dTAG groups at late 2-cell stage. ZGA (n = 2,773) and maternal genes (n = 3,701) were defined. (**e**) Bubble plot showing the overlap between differentially expressed genes and the selected categories. Adjusted *p*-value: hypergeometric test. (**f**) Genome browser views of example genes that are enriched for H3K27me3 in late 2-cell embryos and are de-repressed upon rapid EED depletion. (**g**) Immunostaining images showing rapid depletion of EED and H3K27me3 in morulae after dTAG13 treatment starting from 4-cell stage. DNA, Hoechst 33342. Scale bar, 20 μm. (**h**) Scatter plot comparing gene expression changes between DMSO and dTAG groups at morula stage. (**i**) Bar plots showing the expression changes of representative ICM- and TE-specific genes in DMSO and dTAG groups at morula stage. (**j**) Gene ontology terms enriched for the differentially expressed genes in the dTAG group at morula stage. (**k**) Genome browser views of example genes that are enriched for H3K27me3 in morulae and are de-repressed upon rapid EED depletion.

bioRxiv preprint doi: https://doi.org/10.64898/2026.01.20.700679; this version posted January 20, 2026. The copyright holder for this preprint (which was not certified by peer review) is the author/funder, who has granted bioRxiv a license to display the preprint in perpetuity. It is made available under a CC-BY 4.0 International license.

Fig. 3



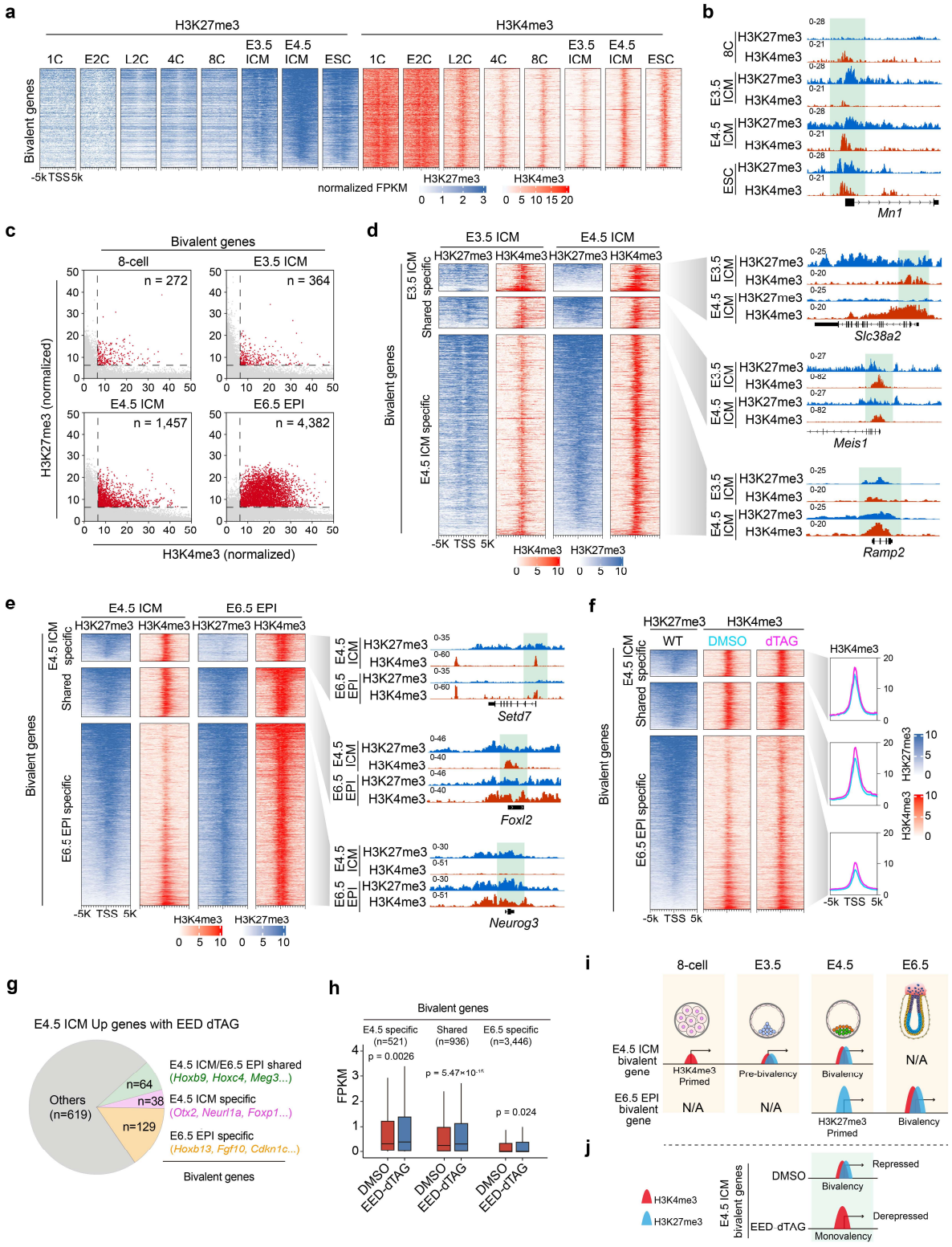
bioRxiv preprint doi: https://doi.org/10.64898/2026.01.20.700679; this version posted January 20, 2026. The copyright holder for this preprint (which was not certified by peer review) is the author/funder, who has granted bioRxiv a license to display the preprint in perpetuity. It is made available under a CC-BY 4.0 International license.

Figure 3. Effects of EED rapid depletion on lineage specification in late blastocysts

(**a**) Schematic showing the dTAG13 treatment strategies for evaluating EED function in lineage specification in late blastocysts. (**b**) Immunostaining images showing the rapid depletion of EED and H3K27me3 in late blastocysts after dTAG13 treatment starting from morula (E2.5-dTAG) or early blastocyst (E3.5-dTAG) stages. DNA, Hoechst 33342. Scale bar, 20 μm. (**c**) Immunostaining images showing the EPI ($NANOG^+/GATA4^-$) and PrE ($GATA4^+/NANOG^-$) cells at late blastocyst stage in DMSO and dTAG groups. EPI: epiblast; PrE: primitive endoderm. Hoechst 33342. Scale bar, 20 μm. (**d**) Quantifications of EPI and PrE cells of panel c (DMSO, n=20; E2.5-dTAG, n=26; E3.5-dTAG, n=24). *p* values were calculated with Student's *t*-test (two-sided). Experiments were repeated three times. (**e**) Scatter plots comparing gene expression changes between DMSO and dTAG groups for E4.5 ICM cells. Red and blue dots represent up- and down-regulated genes in the dTAG group, respectively. (**f**) Gene ontology terms enriched for the differentially expressed genes in the dTAG group for E4.5 ICM cells. (**g**) Bar plots showing the expression changes of representative formative markers, differentiation markers, and *Hox* genes in DMSO and dTAG groups for E4.5 ICM cells. (**h**) Genome browser views of example genes that are enriched with H3K27me3 in E3.5/E4.5 ICM and are de-repressed upon rapid EED depletion. (**i**) Meta plots and heatmaps showing the changes of RNA, H2Aub, H3K4me3, and ATAC signals in E4.5 ICM upon EED depletion. The up-regulated genes in the dTAG group are classified into two groups based on whether H3K27me3 is enriched. (**j**) Genome browser views showing the changes of H2Aub, H3K4me3, ATAC, and RNA signals at *Otx2* and *Bmp2k* loci in E4.5 ICM cells upon rapid EED depletion. (**k**) Meta plots and heatmaps showing the changes of RNA, H2Aub, H3K4me3, and ATAC signals at *Hox* loci in E4.5 ICM upon EED depletion. (**l**) Genome browser views showing the changes of H2Aub, H3K4me3, ATAC, and RNA signals at the *Hoxa* and *Hoxc* loci in E4.5 ICM cells upon rapid EED depletion.

bioRxiv preprint doi: https://doi.org/10.64898/2026.01.20.700679; this version posted January 20, 2026. The copyright holder for this preprint (which was not certified by peer review) is the author/funder, who has granted bioRxiv a license to display the preprint in perpetuity. It is made available under a CC-BY 4.0 International license.

Fig. 4



bioRxiv preprint doi: https://doi.org/10.64898/2026.01.20.700679; this version posted January 20, 2026. The copyright holder for this preprint (which was not certified by peer review) is the author/funder, who has granted bioRxiv a license to display the preprint in perpetuity. It is made available under a CC-BY 4.0 International license.

Figure 4. Effects of EED rapid depletion on bivalency formation in pre- and early post-implantation embryos

(**a**) Dynamics of H3K27me3 and H3K4me3 at bivalent genes identified in E4.5 ICM (n = 1457, Methods) throughout preimplantation development. (**b**) Genome browser views of H3K27me3 and H3K4me3 dynamics at an example bivalent locus from 8-cell to E4.5 ICM and ESCs. (**c**) Scatter plot showing the number of bivalent genes (red dots) at the indicated developmental stages. (**d**) Dynamics of H3K27me3 and H3K4me3 at bivalent loci during the E3.5 ICM to E4.5 ICM transition. Left panel showing heatmaps of these two histone modifications in E3.5 ICM and E4.5 ICM cells. All bivalent loci are classified into three groups: "E3.5 ICM specific", "Shared", and "E4.5 ICM specific". Right panel showing genome browser views of example genes for each group. (**e**) Dynamics of H3K27me3 and H3K4me3 at bivalent loci during the E4.5 ICM to E6.5 EPI transition. Left panel showing heatmaps of these two histone modifications in E4.5 ICM and E6.5 ICM cells. All bivalent loci are classified into three groups: "E4.5 ICM specific", "Shared", and "E6.5 ICM specific". Right panel showing genome browser views of example genes for each group. (**f**) Effects of EED rapid depletion on H3K4me3 at bivalent loci in E4.5 ICM. Left panel showing heatmaps of H3K27me3 and the changes of H3K4me3 upon EED depletion. Right panel showing the metaplots that summarizing average H3K4me3 signals at the bivalent genes. (**g**) Pie chart showing the bivalent genes that are up regulated in E4.5 ICM upon EED depletion. (**h**) Boxplot showing the RNA expression changes of different groups of bivalent genes upon EED depletion in E4.5 ICM cells. *P*-values are calculated with two-sided Wilcoxon signed rank test. In the boxplot, the central band represents the median. The lower and upper edges of the box represent the first and third quartiles, respectively. The whiskers of the boxplot extend to 1.5 times interquartile range (IQR). (**i**) Schematic model summarizing the dynamics of H3K4me3 and H3K27me3 at bivalent loci during the 8-cell to E3.5/E4.5 ICM and E4.5 ICM to E6.5 EPI transitions. (**j**) Schematic model summarizing the impact of EED rapid depletion on H3K4me3 and H3K27me3 at bivalent genes in E4.5 ICM cells.

bioRxiv preprint doi: https://doi.org/10.64898/2026.01.20.700679; this version posted January 20, 2026. The copyright holder for this preprint (which was not certified by peer review) is the author/funder, who has granted bioRxiv a license to display the preprint in perpetuity. It is made available under a CC-BY 4.0 International license.

Fig. 5

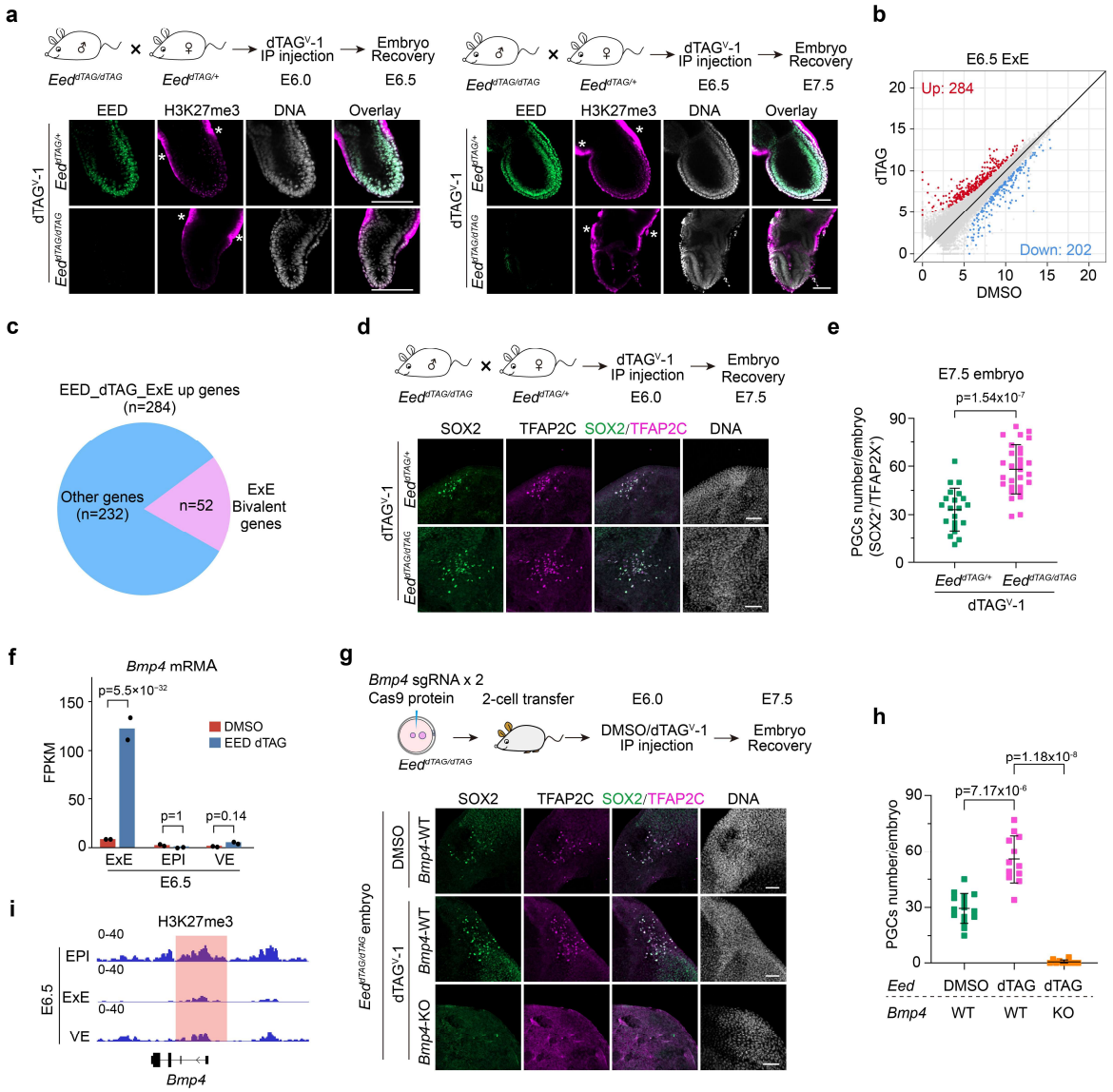


Figure 5. EED depletion during gastrulation causes primordial germ cells (PGCs) increase through BMP4 signaling

(**a**) Immunostaining images showing the rapid depletion of EED and H3K27me3 in post-implantation embryos (*i.e.,* E6.5 or E7.5) following administration of dTAG^{V}-1 by Intraperitoneal (IP) injection. All embryos were collected, subjected to genotyping, and then processed for downstream analysis. Hoechst 33342. Scale bar, 100 μm. *showed the non-specific staining of H3K27me3. **(b)** Scatter plot comparing gene expression changes between DMSO and dTAG groups in E6.5 ExE. For the RNA-seq, EED degradation was performed at E5.5. **(c)** Pie chart showing the number of ExE bivalent genes in the up-

bioRxiv preprint doi: https://doi.org/10.64898/2026.01.20.700679; this version posted January 20, 2026. The copyright holder for this preprint (which was not certified by peer review) is the author/funder, who has granted bioRxiv a license to display the preprint in perpetuity. It is made available under a CC-BY 4.0 International license.

regulated genes upon EED depletion. (**d**) Immunostaining images showing the increased PGCs ($SOX2^+/TFAP2C^+$) in E7.5 embryos after EED depletion. Hoechst 33342. Scale bar, 100 μm. (**e**) Quantification of PGCs in panel d ($Eed^{dTAG/+}$, n=21; $Eed^{dTAG/dTAG}$, n=29). *p* values were calculated with Student's *t*-test (two-sided). Experiments were repeated three times. (**f**) Bar plot showing the RNA expression changes of *Bmp4* after EED depletion in E6.5 EPI, ExE, and VE. The adjusted *p*-value was calculated by DESeq2. (**g**) Top panel: schematic showing the experimental design to evaluate how acute *Bmp4* KO may affect PGCs with or without dTAG-mediated EED depletion in E7.5 embryos; Bottom panel: immunostaining images showing the number of PGCs in E7.5 embryos following EED single depletion or EED/BMP4 double depletion. Hoechst 33342. Scale bar, 100 μm. (**h**) Quantification of PGCs in panel g (*Eed*-DMSO/*Bmp4*-WT, n=15; *Eed*-dTAG/*Bmp4*-WT, n=12; *Eed*-dTAG/*Bmp4*-KO, n=11). *p* values were calculated with Student's *t*-test (two-sided). Experiments were repeated three times. (**i**) Genome browser view of H3K27me3 at the *Bmp4* locus in E6.5 EPI, ExE and VE lineages.

bioRxiv preprint doi: https://doi.org/10.64898/2026.01.20.700679; this version posted January 20, 2026. The copyright holder for this preprint (which was not certified by peer review) is the author/funder, who has granted bioRxiv a license to display the preprint in perpetuity. It is made available under a CC-BY 4.0 International license.

Fig. 6

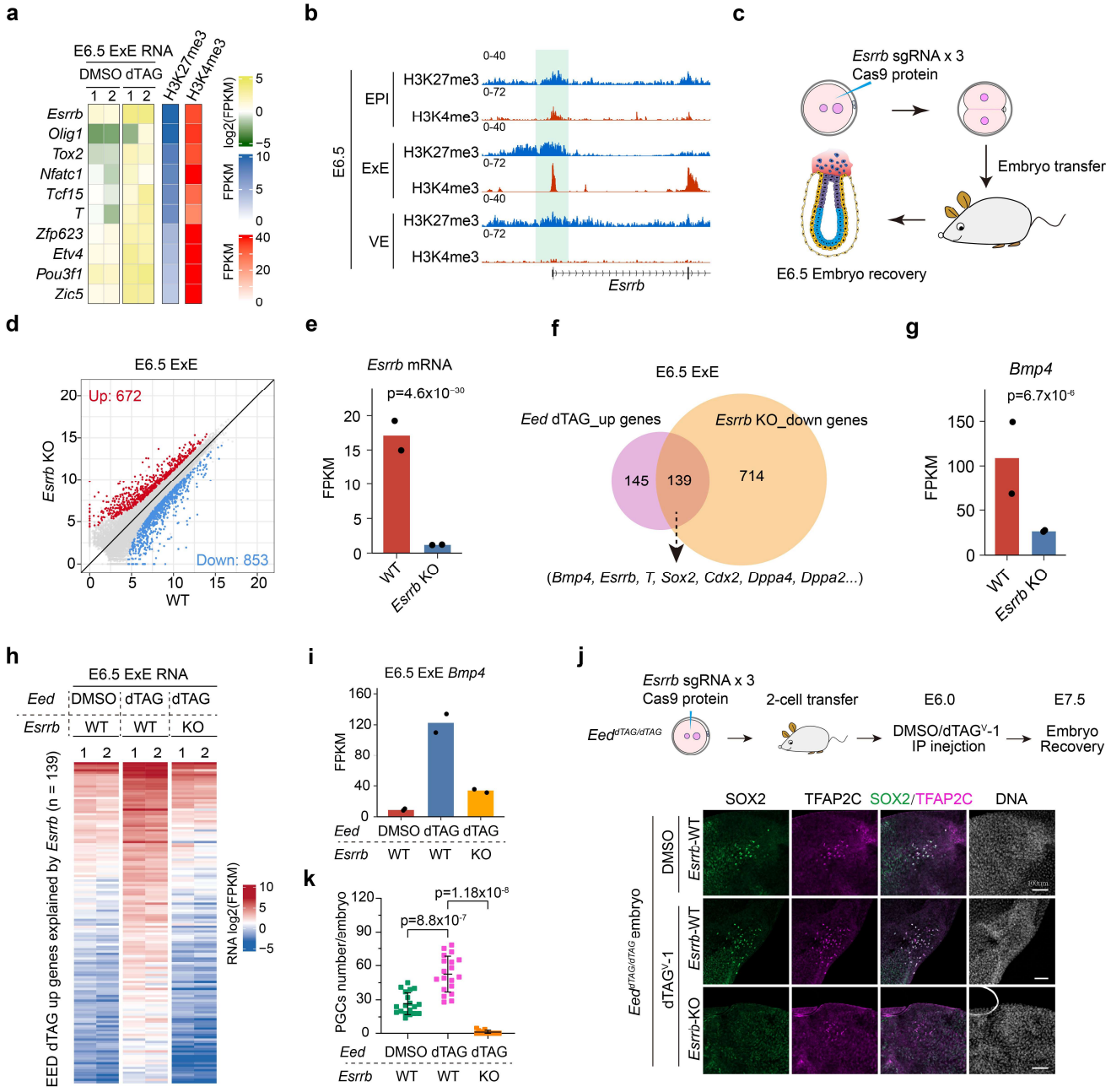


Figure 6. EED suppresses PGC fate by directly repressing *Esrrb*

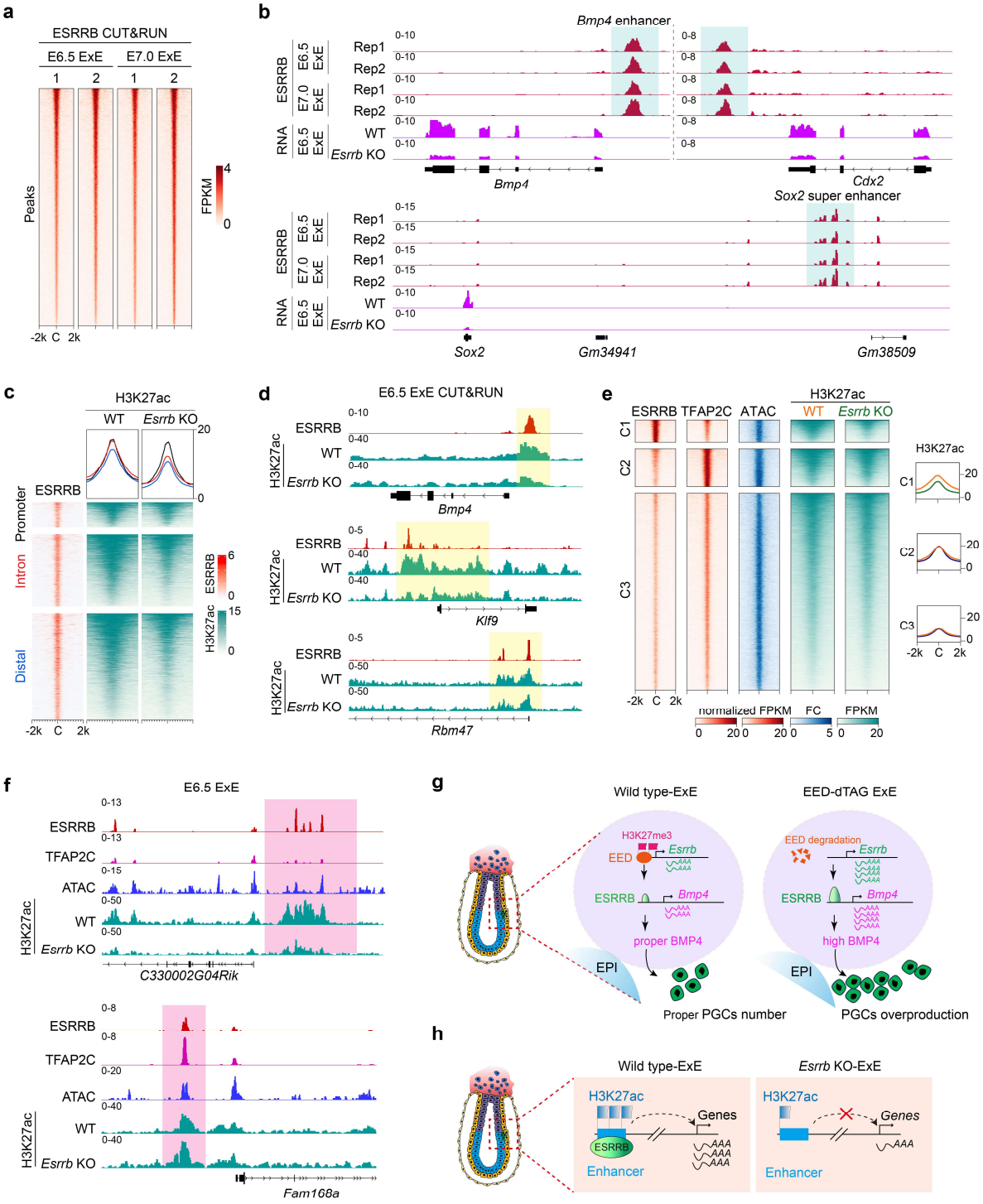
(**a**) Heatmap showing RNA, H3K27me3 and H3K4me3 levels of the candidate bivalent TFs that may be involved in PGC specification in E6.5 ExE. (**b**) Genome browser views of H3K4me3 and H3K27me3 at the *Esrrb* locus in E6.5 EPI, ExE, and VE lineages. (**c**) Schematic showing the experimental design for

bioRxiv preprint doi: https://doi.org/10.64898/2026.01.20.700679; this version posted January 20, 2026. The copyright holder for this preprint (which was not certified by peer review) is the author/funder, who has granted bioRxiv a license to display the preprint in perpetuity. It is made available under a CC-BY 4.0 International license.

acute *Esrrb* KO by zygotic CRISPR injection. (**d**) Scatter plot comparing gene expression changes between *Esrrb* wild type (WT) and KO E6.5 ExE. (**e**) Bar plot showing the RNA expression changes of *Esrrb* in *Esrrb* KO E6.5 ExE. The adjusted *p*-value was calculated by DESeq2. (**f**) Venn diagram showing the overlap of genes that are de-repressed upon EED depletion and genes that are down-regulated by *Esrrb* KO in E6.5 ExE. (**g**) Bar plot showing the RNA expression changes of *Bmp4* in E6.5 ExE after *Esrrb* KO. The adjusted *p*-value was calculated by DESeq2. (**h**) Heatmap illustrating the RNA expression changes of the 139 genes that are de-repressed by EED depletion but are down-regulated in E6.5 ExE of *Esrrb* KO. (**i**) Bar plot showing the RNA expression changes of *Bmp4* in E6.5 ExE following EED single depletion or EED/ESRRB double depletion. (**j**) Top panel: schematic showing the experimental design to evaluate how acute KO of *Esrrb* may affect PGC numbers with or without EED depletion in E7.5 embryos; Bottom panel: immunostaining images showing the number of PGCs in E7.5 embryos following EED single depletion or EED/ESRRB double depletion. Hoechst 33342. Scale bar, 100 μm. (**k**) Quantification of PGC numbers in panel j (*Eed*-DMSO/*Esrrb*-WT, n=19; *Eed*-dTAG/*Esrrb*-WT, n=19; *Eed*-dTAG/*Esrrb*-KO, n=14). *p* values were calculated with Student's *t*-test (two-sided). Experiments were repeated three times.

bioRxiv preprint doi: https://doi.org/10.64898/2026.01.20.700679; this version posted January 20, 2026. The copyright holder for this preprint (which was not certified by peer review) is the author/funder, who has granted bioRxiv a license to display the preprint in perpetuity. It is made available under a CC-BY 4.0 International license.

994 **Fig. 7**



995

996

997

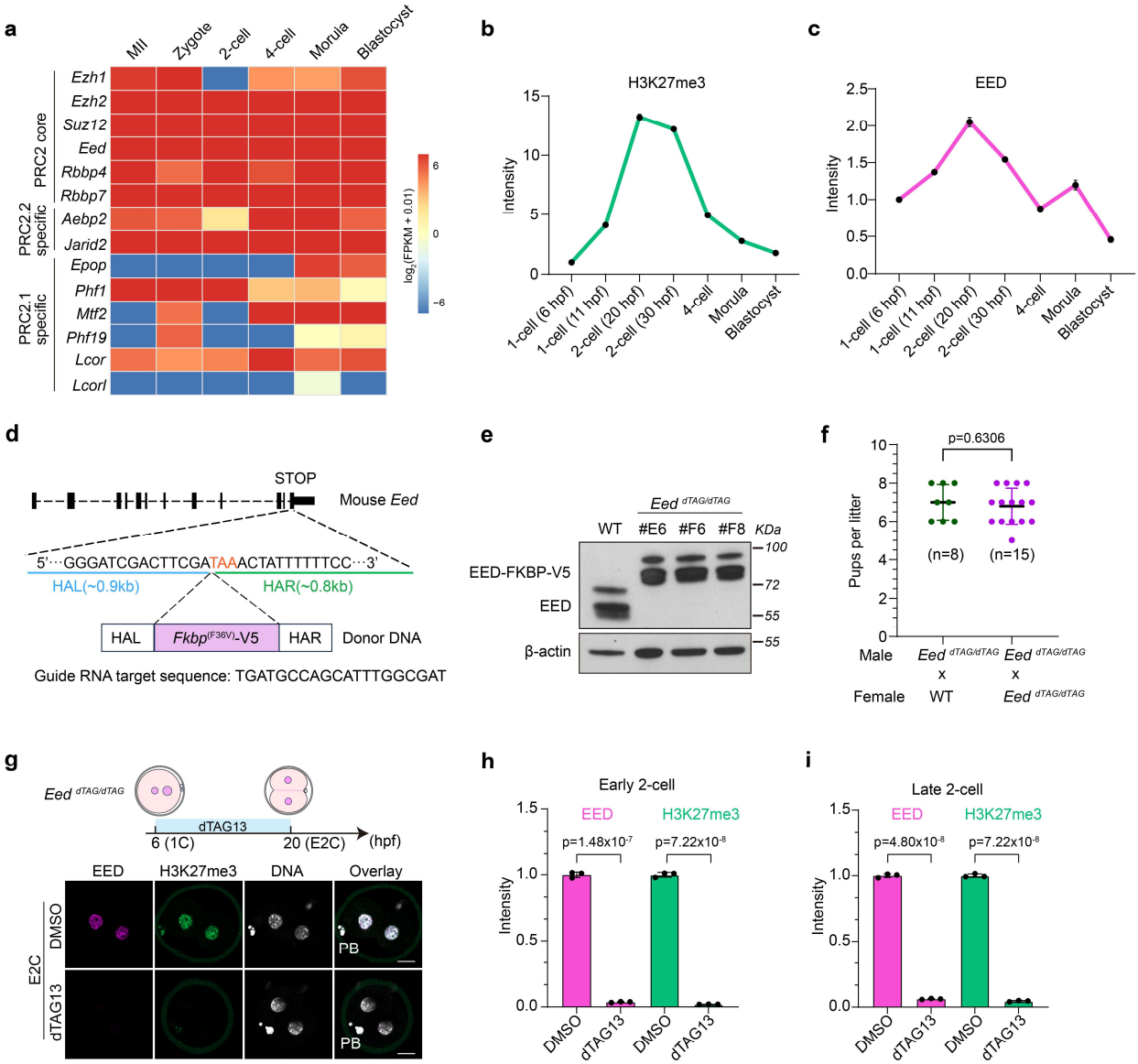
bioRxiv preprint doi: https://doi.org/10.64898/2026.01.20.700679; this version posted January 20, 2026. The copyright holder for this preprint (which was not certified by peer review) is the author/funder, who has granted bioRxiv a license to display the preprint in perpetuity. It is made available under a CC-BY 4.0 International license.

Figure 7. ESRRB regulates gene expression in ExE through binding to enhancers

(**a**) Heatmap illustrating ESRRB CUT&RUN signals in E6.5 and E7.0 ExE. Two biological replicates for each stage are shown. (**b**) Genome browser views of ESRRB binding and RNA signals at the indicated genomic loci. (**c**) Heatmap showing the H3K27ac changes caused by *Esrrb* KO at ESRRB-bound promoters, introns, and distal regions in E6.5 ExE. (**d**) Genome browser views of ESRRB binding and H3K27ac changes at the indicated genomic loci. (**e**) Left panel: heatmaps showing ATAC signal and the H3K27ac changes caused by *Esrrb* KO at ESRRB and TFAP2C co-bound regions. The peaks were classified into three clusters based on ESRRB and TFAP2C enrichment levels. (**f**) Genome browser views of ESRRB and TFAP2C binding, ATAC signal, and H3K27ac level at the indicated genomic loci. (**g**) Diagram summarizing the EED-ESRRB-BMP4 axis in regulating PGC specification during gastrulation. (**h**) Diagram illustrating that ESRRB regulates its target genes by activating enhancers.

bioRxiv preprint doi: https://doi.org/10.64898/2026.01.20.700679; this version posted January 20, 2026. The copyright holder for this preprint (which was not certified by peer review) is the author/funder, who has granted bioRxiv a license to display the preprint in perpetuity. It is made available under a CC-BY 4.0 International license.

Extended Data Figures



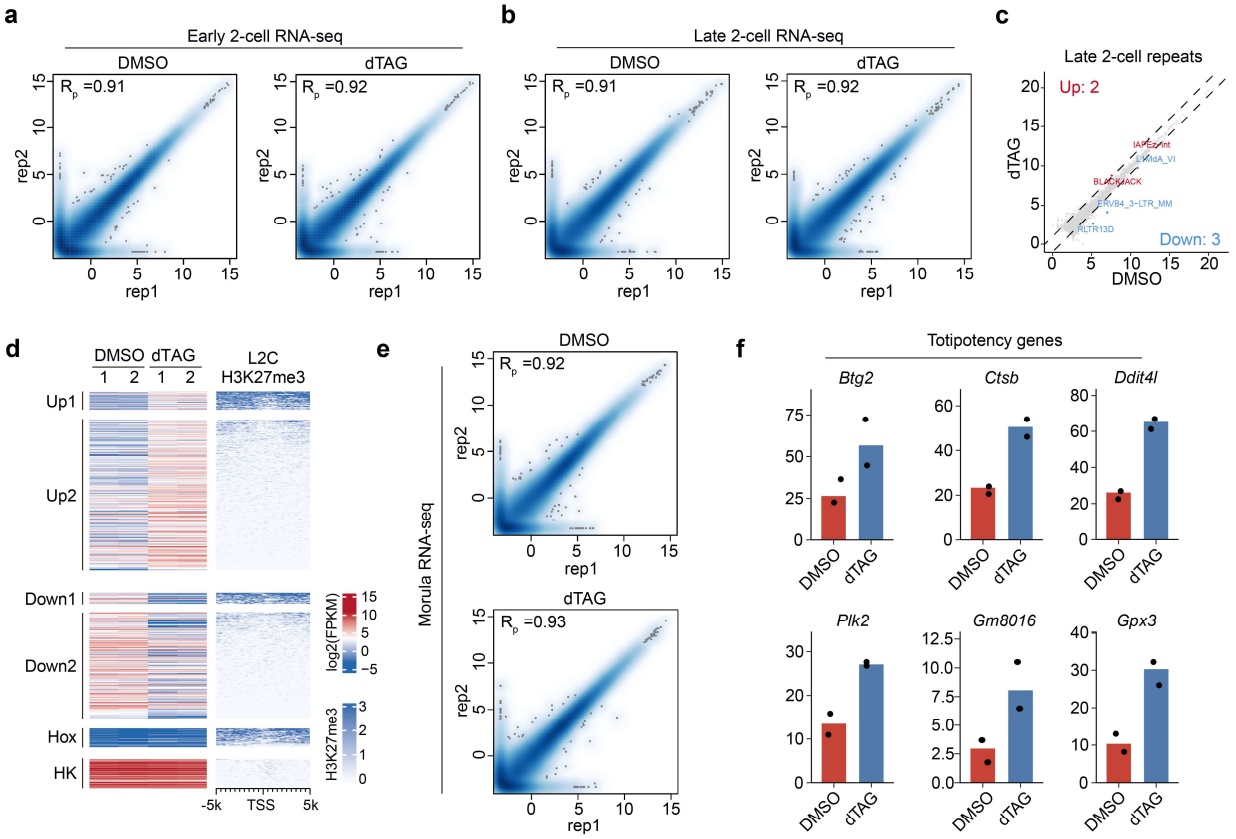
Extended Data Figure 1. Generation and characterization of the *Eed* dTAG mouse model

(**a**) Ribosome profiling signals of PRC2 core and accessory subunits during pre-implantation development. MII: metaphase II eggs; FPKM: fragments per kilobase per million mapped reads. (**b-c**) Quantification of the H3K27me3 (**b**) and EED (**c**) immunostaining signals in preimplantation embryos. hpf: hrs post fertilization. (**d**) Schematic showing the dTAG knock-in design at the *Eed* locus. HAL: left homology arm; HAR: right homology arm. (**e**) Immunoblotting images showing the wild type (WT) EED and EED-dTAG proteins in mouse embryonic stem cells. The blots were incubated with anti-EED. β-Actin was used as a loading control. (**f**) Litter sizes of the breeding crosses. Number of litters analyzed are shown. The *p* value

bioRxiv preprint doi: https://doi.org/10.64898/2026.01.20.700679; this version posted January 20, 2026. The copyright holder for this preprint (which was not certified by peer review) is the author/funder, who has granted bioRxiv a license to display the preprint in perpetuity. It is made available under a CC-BY 4.0 International license.

was calculated with Student's *t*-test (two-sided). Data are presented as mean values ± SD. (**g**) Immunostaining images showing the rapid depletion of EED and H3K27me3 in early 2-cell embryos after dTAG13 treatment starting from zygotes. PB, polar body. DNA, Hoechst 33342. Scale bar, 20 μm. (**h-i**) Quantification of EED (**h**) and H3K27me3 (**i**) immunostaining signals in early 2-cell embryos. Experiments were repeated three times. *p* values were calculated with Student's *t*-test (two-sided). Data are presented as mean values ± SD.

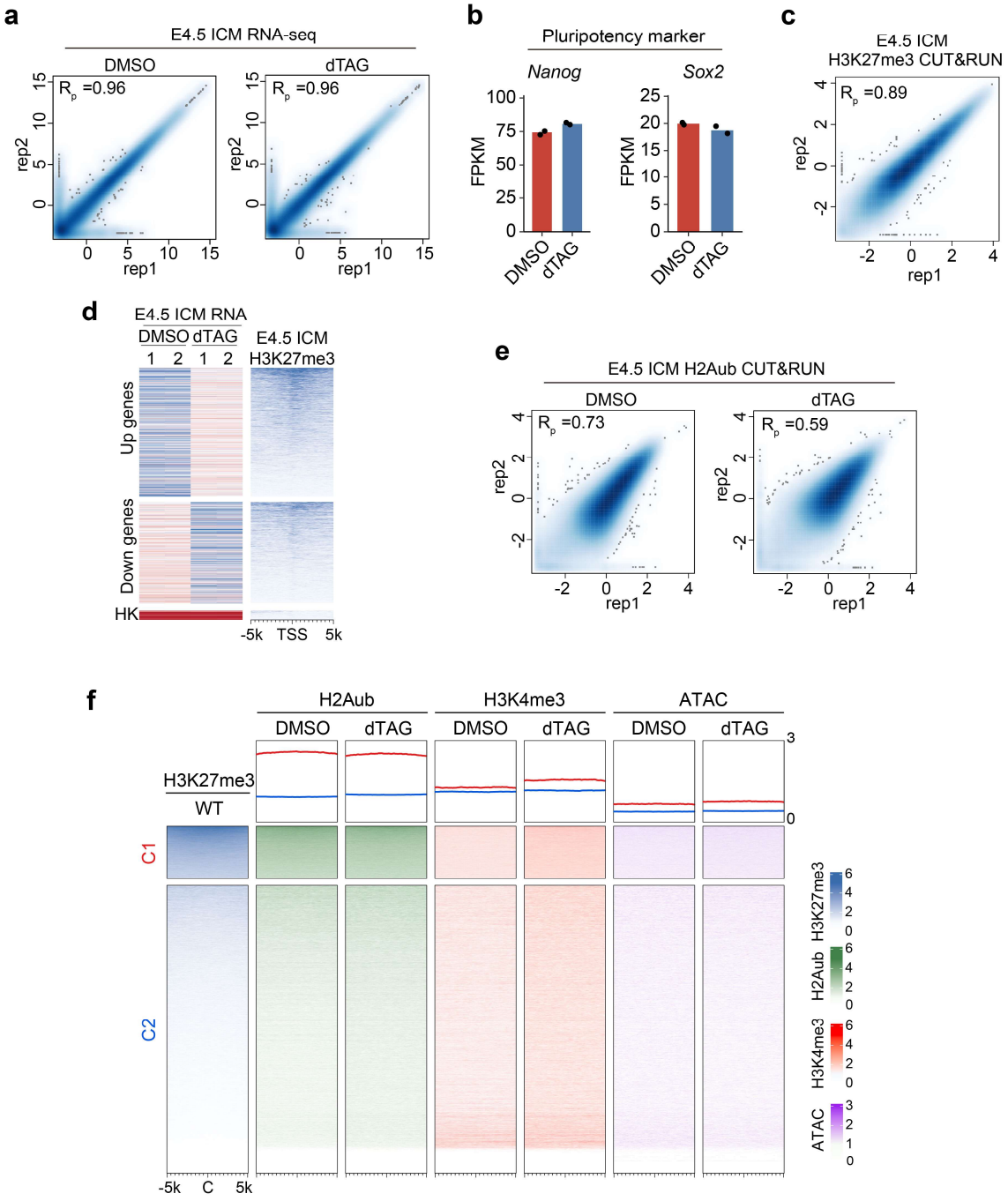
bioRxiv preprint doi: https://doi.org/10.64898/2026.01.20.700679; this version posted January 20, 2026. The copyright holder for this preprint (which was not certified by peer review) is the author/funder, who has granted bioRxiv a license to display the preprint in perpetuity. It is made available under a CC-BY 4.0 International license.



Extended Data Figure 2. Transcriptome analyses of the *Eed* dTAG embryos at early 2-cell, late 2-cell, and morula stages

(**a-b**) Scatter plots showing the reproducibility between biological replicates for early (**a**) and late 2-cell (**b**) RNA-seq datasets. Pearson correlation coefficients are shown. (**c**) Scatter plot comparing repeat expression changes between DMSO and dTAG groups at late 2-cell stage. Red and blue dots represent up- and down-regulated repeat subfamilies in the dTAG group, respectively. The cutoff used to define differentially expressed repeats: fold change (FC) >= 2, and adjusted *p*-value < 0.05. (**d**) Heatmap illustrating RNA and H3K27me3 levels for the differentially expressed genes in the late 2-cell embryos. Hox and housekeeping (HK) genes serve as the positive and negative controls for H3K27me3, respectively. (**e**) Scatter plots showing the reproducibility between biological replicates for morula RNA-seq datasets. Pearson correlation coefficients are shown. (**f**) Bar plots showing the expression changes of representative totipotency genes in DMSO and dTAG groups at morula stage.

bioRxiv preprint doi: https://doi.org/10.64898/2026.01.20.700679; this version posted January 20, 2026. The copyright holder for this preprint (which was not certified by peer review) is the author/funder, who has granted bioRxiv a license to display the preprint in perpetuity. It is made available under a CC-BY 4.0 International license.



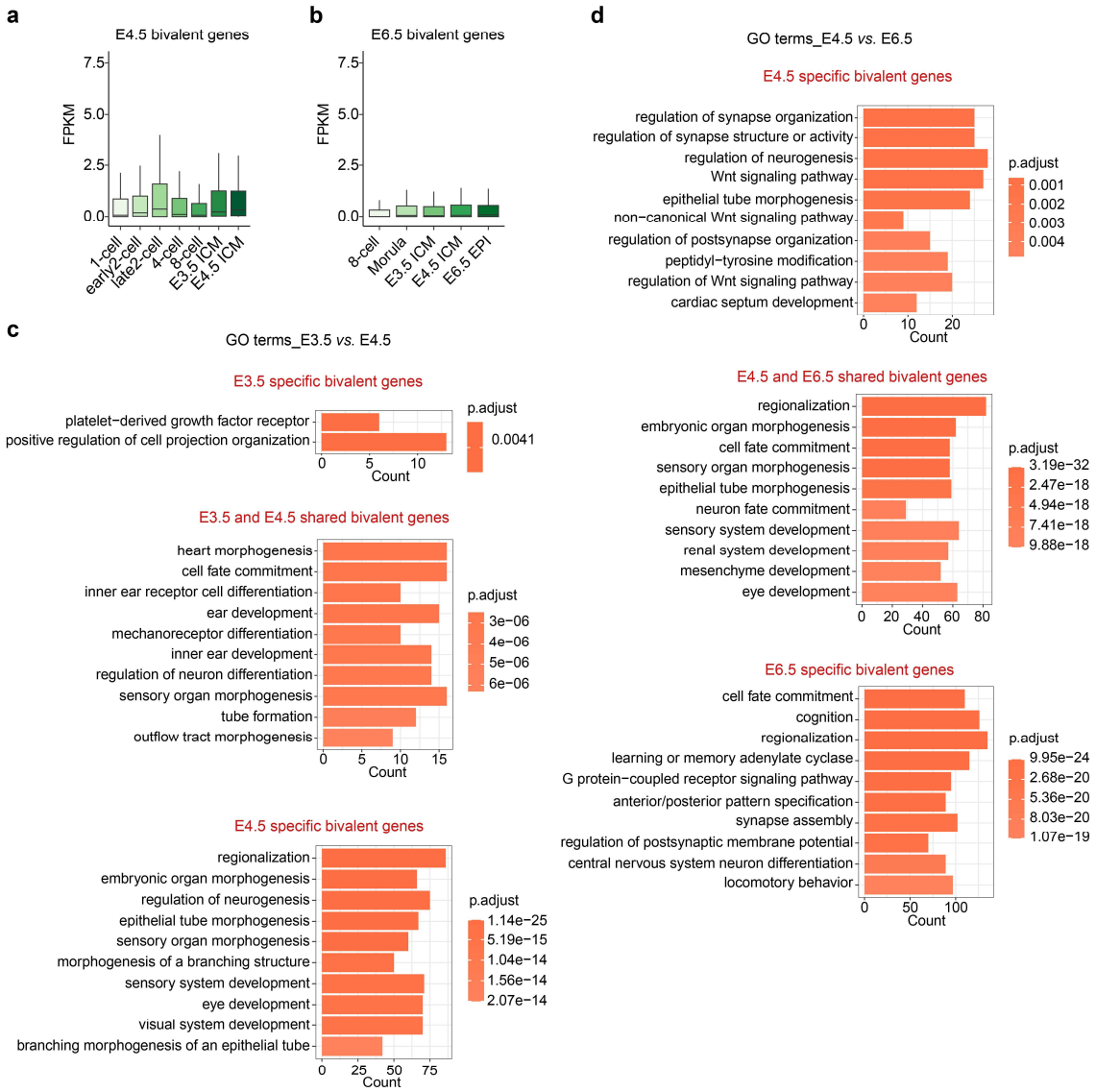
Extended Data Figure 3. Transcriptome and chromatin analyses of E4.5 inner cell mass (ICM) cells

(**a**) Scatter plots showing the reproducibility between biological replicates for E4.5 ICM RNA-seq datasets. Pearson correlation coefficients are shown. (**b**) Bar plots showing the expression changes of representative pluripotent markers in DMSO and dTAG groups of E4.5 ICM cells. (**c**) Scatter plots showing the

bioRxiv preprint doi: https://doi.org/10.64898/2026.01.20.700679; this version posted January 20, 2026. The copyright holder for this preprint (which was not certified by peer review) is the author/funder, who has granted bioRxiv a license to display the preprint in perpetuity. It is made available under a CC-BY 4.0 International license.

reproducibility between biological replicates for H3K27me3 CUT&RUN datasets. Pearson correlation coefficient is shown. (**d**) Heatmap illustrating RNA and H3K27me3 levels for the differentially expressed genes in E4.5 ICM cells. Housekeeping (HK) genes serve as negative controls for H3K27me3. (**e**) Scatter plots showing the reproducibility between biological replicates for E4.5 ICM H2Aub CUT&RUN datasets. Pearson correlation coefficients are shown. (**f**) Heatmap showing genome-wide 10 kb bins of signals for H2Aub, H3K4me3 and ATAC-seq peaks in E4.5 ICM with or without EED degradation. All the bins were classified into two subgroups based on the level of H3K27me3. C: peak center.

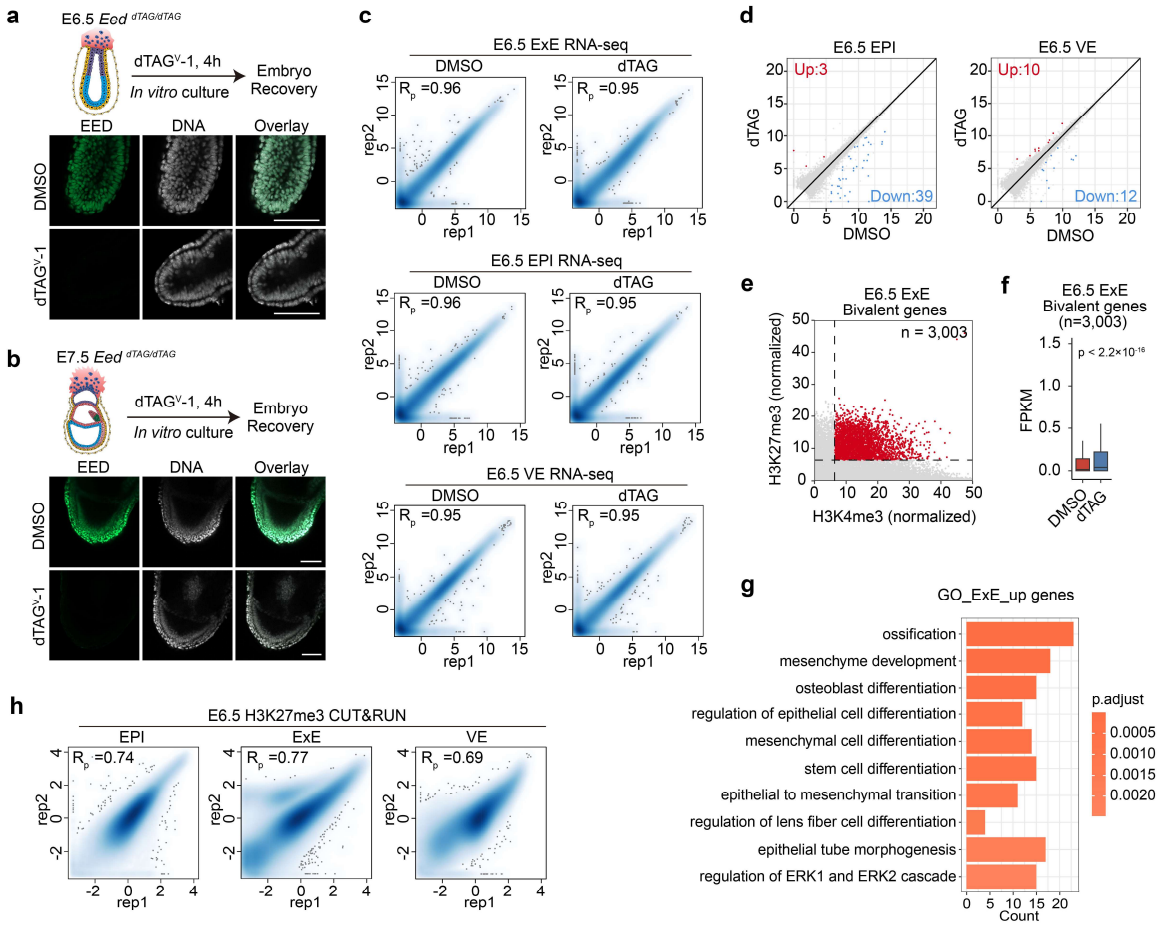
bioRxiv preprint doi: https://doi.org/10.64898/2026.01.20.700679; this version posted January 20, 2026. The copyright holder for this preprint (which was not certified by peer review) is the author/funder, who has granted bioRxiv a license to display the preprint in perpetuity. It is made available under a CC-BY 4.0 International license.



Extended Data Figure 4. Bivalent gene analyses at different development stages

(**a-b**) Boxplots showing the E4.5 ICM (**a**) and E6.5 EPI (**b**) bivalent gene expressions in pre- and peri-implantation embryos. In the boxplot, the central band represents the median. The lower and upper edges of the box represent the first and third quartiles, respectively. The whiskers of the boxplot extend to 1.5 times interquartile range (IQR). (**c-d**) Gene ontology (GO) term analyses for the indicated bivalent gene groups.

bioRxiv preprint doi: https://doi.org/10.64898/2026.01.20.700679; this version posted January 20, 2026. The copyright holder for this preprint (which was not certified by peer review) is the author/funder, who has granted bioRxiv a license to display the preprint in perpetuity. It is made available under a CC-BY 4.0 International license.



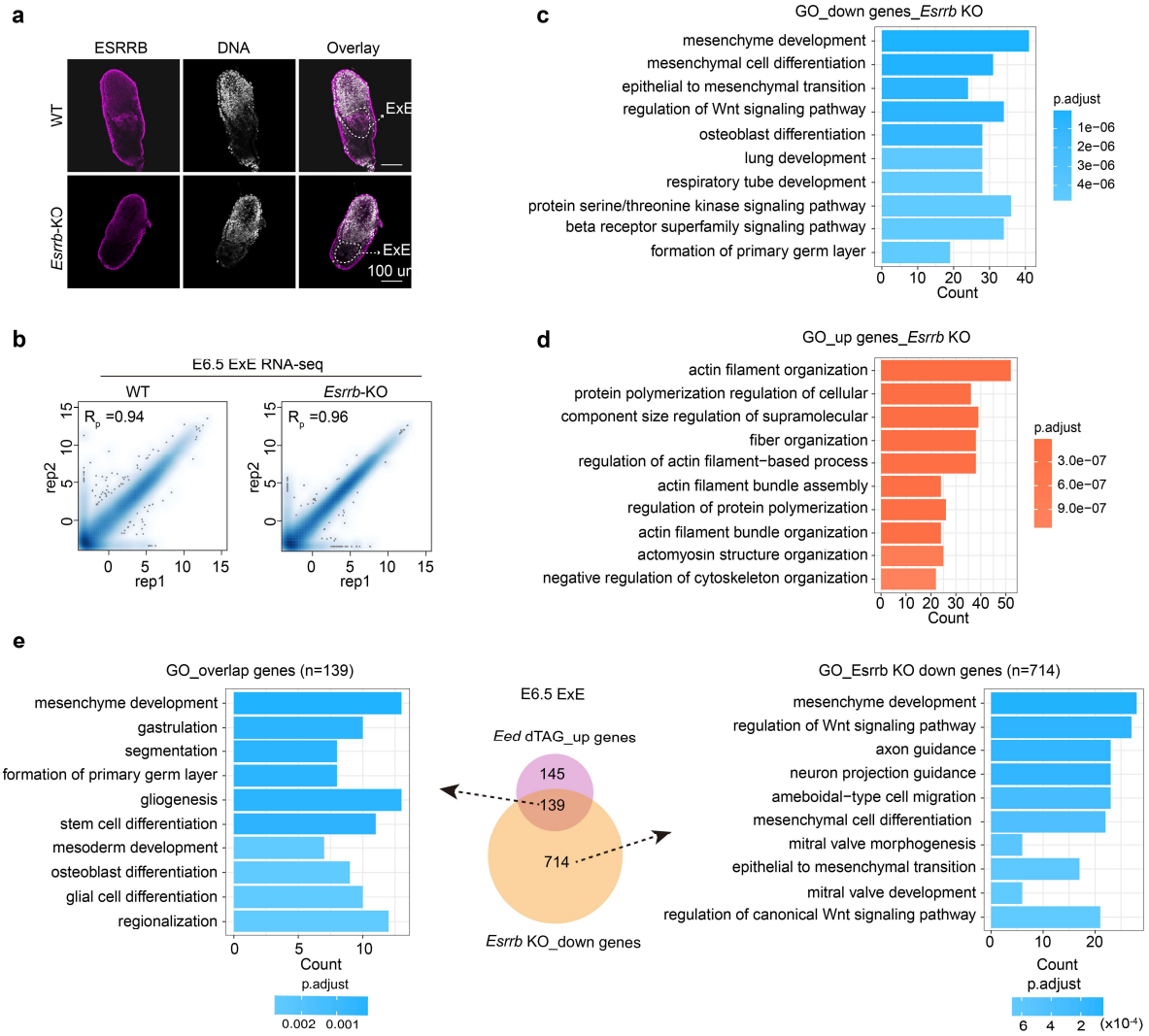
Extended Data Figure 5. Rapid degradation in EED in early post-implantation embryos

(**a-b**) Immunostaining images showing the rapid depletion of EED in *ex vivo* cultured E6.5 (**a**) and E7.5 (**b**) post-implantation embryos following 4 hr treatment with dTAG^{V}-1. Hoechst 33342. Scale bar, 100 μm. (**c**) Scatter plots showing the reproducibility between biological replicates for E6.5 EPI, ExE, and VE RNA-seq datasets. Pearson correlation coefficients are shown. (**d**) Scatter plot comparing gene expression changes between DMSO and dTAG groups in E6.5 EPI and VE. Red and blue dots represent up- and down-regulated repeat subfamilies in the dTAG group, respectively. The cutoff used to define differentially expressed repeats: fold change (FC) >= 2, adjusted *p*-value < 0.05 and FPKM >= 1. (**e**) Scatter plot showing the number of bivalent genes (red dots) in E6.5 ExE. (**f**) Boxplot showing the E6.5 ExE bivalent gene expressions changes between DMSO and dTAG groups. In the boxplot, the central band represents the median. The lower and upper edges of the box represent the first and third quartiles, respectively. The whiskers of the boxplot extend to 1.5 times interquartile range (IQR). *P*-values were calculated with two-sided Wilcoxon signed rank test. (**g**) GO term analyses for the up-regulated genes in E6.5 ExE upon EED

bioRxiv preprint doi: https://doi.org/10.64898/2026.01.20.700679; this version posted January 20, 2026. The copyright holder for this preprint (which was not certified by peer review) is the author/funder, who has granted bioRxiv a license to display the preprint in perpetuity. It is made available under a CC-BY 4.0 International license.

depletion. (**h**) Scatter plots showing the reproducibility between biological replicates for H3K27me3 CUT&RUN datasets. Pearson correlation coefficients are shown.

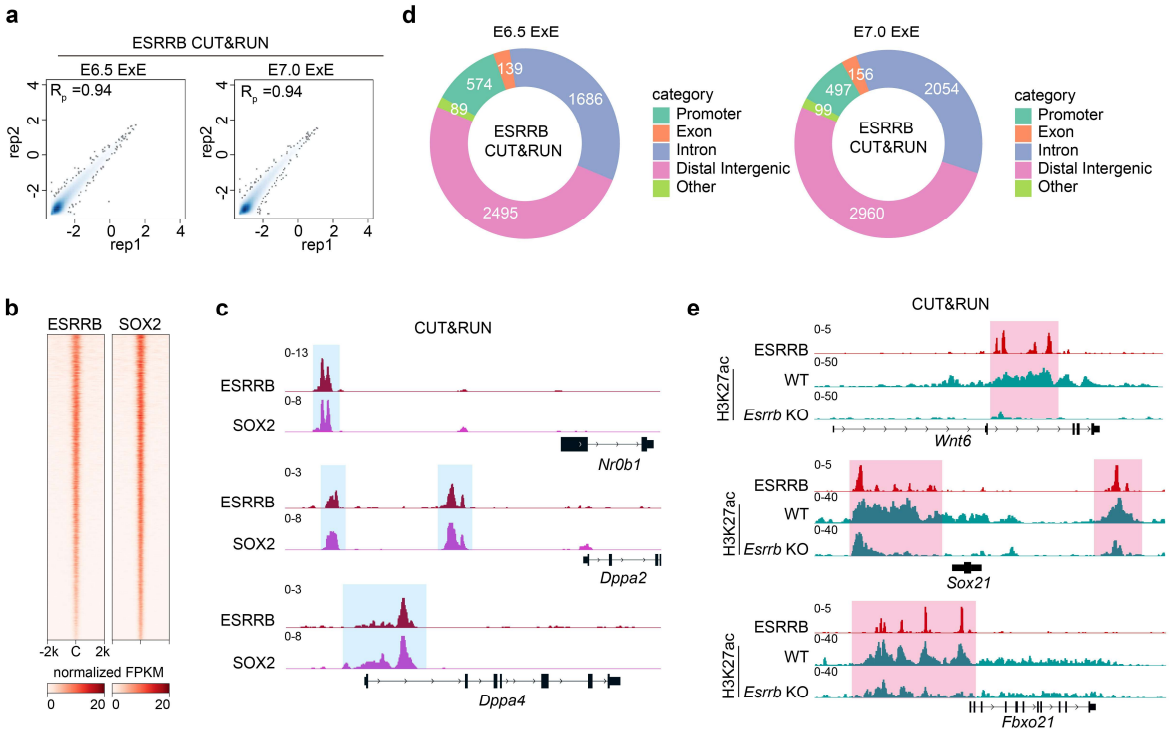
bioRxiv preprint doi: https://doi.org/10.64898/2026.01.20.700679; this version posted January 20, 2026. The copyright holder for this preprint (which was not certified by peer review) is the author/funder, who has granted bioRxiv a license to display the preprint in perpetuity. It is made available under a CC-BY 4.0 International license.



Extended Data Figure 6. Transcriptome analyses of *Esrrb* KO E6.5 ExE

(**a**) Immunostaining images showing the ESRRB signals in WT and *Esrrb* KO embryos at E6.5. The white dashed circles show the EXE lineage. Hoechst 33342. Scale bar, 100 μm. **(b)** Scatter plots showing the reproducibility between biological replicates for E6.5 ExE RNA-seq datasets. Pearson correlation coefficients are shown. (**c-d**) GO term analyses for the down-regulated **(c)** and up-regulated **(d)** genes in E6.5 ExE of *Esrrb* KO embryos. (**e**) Middle: Venn diagram (also shown in Fig. 6f) showing the overlap between the up-regulated genes in E6.5 ExE upon EED depletion and the down-regulated genes in the same lineage of *Esrrb* KO. GO term analyses of the indicated gene sets are shown.

bioRxiv preprint doi: https://doi.org/10.64898/2026.01.20.700679; this version posted January 20, 2026. The copyright holder for this preprint (which was not certified by peer review) is the author/funder, who has granted bioRxiv a license to display the preprint in perpetuity. It is made available under a CC-BY 4.0 International license.



Extended Data Figure 7. ESRRB CUT&RUN analyses in ExE cells

(**a**) Scatter plots showing the reproducibility between biological replicates for E6.5 and E7.0 ExE ESRRB CUT&RUN datasets. Pearson correlation coefficients are shown. (**b**) Heatmap showing the ESRRB and SOX2 binding at E6.5 ExE lienage. C: peak centers. (**c**) Examples of ExE developmental genes with both ESRRB and SOX2 binding (shaded) at E6.5 ExE lineage. (**d**) Pie chart showing the ESRRB peaks distributions in E6.5 and E7.0 ExE. (**e**) Genome browser views of ESRRB and H3K27ac signals (shaded) in E6.5 ExE of WT and *Esrrb* KO embryos.

bioRxiv preprint doi: https://doi.org/10.64898/2026.01.20.700679; this version posted January 20, 2026. The copyright holder for this preprint (which was not certified by peer review) is the author/funder, who has granted bioRxiv a license to display the preprint in perpetuity. It is made available under a CC-BY 4.0 International license.

Supplementary Tables

Supplementary Table 1. Gene lists used in this study.

Supplementary Table 2. Differential expressed genes of early 2-cell, late 2-cell and morula treated with EED dTAG13 versus that treated with DMSO.

Supplementary Table 3. Differential expressed genes of E4.5 ICM treated with EED dTAG13 versus that treated with DMSO.

Supplementary Table 4. Bivalent genes in E3.5 ICM, E4.5 ICM, E6.5 EPI and E6.5 ExE.

Supplementary Table 5. Differential expressed genes in EPI, ExE and VE of E6.5 embryo treated with EED dTAG^{V}-1 versus the control.

Supplementary Table 6. Differential expressed genes in E6.5 ExE with *Esrrb* zygotic KO versus wildtype E6.5 ExE.

Supplementary Table 7. Oligos used in this study.